Optical Analysis of a Linear-Array Thermal Radiation Detector for Geostationary Earth Radiation Budget Applications

by

María Cristina Sánchez C.

Thesis submitted to the faculty of the
Virginia Polytechnic Institute and State University
In partial fulfillment of the requirements for the degree of
Master of Science

In

Mechanical Engineering

Dr. J. R. Mahan, Chairman
Dr. E. P. Scott
Dr. T. E. Diller

March 6, 1998
Blacksburg, Virginia

Keywords: Linear-array thermal radiation detector, Monte-Carlo ray-trace method, cavity effect, optical cross-talk

Optical Analysis of a Linear-Array Thermal Radiation Detector for Geostationary Earth Radiation Budget Applications

By María Cristina Sánchez C.
J. Robert Mahan, Chairman
Mechanical Engineering
(ABSTRACT)

The Thermal Radiation Group, a laboratory in the Department of Mechanical Engineering at Virginia Polytechnic Institute and State University, is currently working to develop a new technology for thermal radiation detectors. The Group is also studying the viability of replacing current Earth Radiation Budget radiometers with this new concept. This next-generation detector consists of a thermopile linear array thermal radiation detector. The principal objective of this research is to develop an optical model for the detector and its cavity. The model based on the Monte-Carlo ray-trace (MCRT) method, permits parametric studies to optimize the design of the detector cavity and the specification of surface optical properties. The model is realized as a FORTRAN program which permits the calculation of quantities related to the cross-talk among pixels of the detector and radiation exchange among surfaces of the cavity. An important capability of the tool is that it provides estimates of the discrete Green's function that permits partial correction for optical cross-talk among pixels of the array.

Agradecimientos

Primero que todo quiero agradecer a mi “advisor” por su confianza ciega, apoyo incondicional e inmensa paciencia, y a Dr E. P. Scott y Dr. T. E. Diller por su disponibilidad para ser miembros de mi comité.

Quiero agradecer también a mis compañeros del Grupo de Radiación Térmica: Katherine, Félix, Ira, Edwin, Joel y Stephanie, a mi paisano Juan Carlos y a los cordobeses Raúl y Sergio, quienes sin su ayuda esto hubiera sido mucho más difícil sino imposible. Al resto de mis amigos, muchas gracias por hacer de mi paso por Blacksburg y Virginia Tech una experiencia placentera y enriquecedora.

Finalmente y de una manera muy especial, agradezco a mis padres y mi hermana por el enorme apoyo y quienes a pesar de la distancia hicieron lo posible por hacerme llegar su cariño y ánimo para seguir adelante.

Table of Contents

List of Tables

List of Figures

Chapter 1. Introduction

A consequence of the emergence of industrialized societies is that related human activity has become a powerful agent for changes in the Earth's environment. Agricultural and industrial revolutions have altered the composition of the atmosphere and have led to the erosion of soils with sediment loading of river beds as a consequence.

The emission of Chlorfluoro-Carbons and the burning of fossil fuels have led to the origin of processes such as the greenhouse effect that have the potential to change the global climate. It is well known that the greenhouse effect has a primary warming influence, but this warming influence also motivates the production of more water vapor (one of the greenhouse gases), which in turn encourages the formation of clouds. Clouds are known to have a net cooling effect, which may to a certain extent counter-balance the heating effect.

In order to understand all of these changes and their causes, the international scientific community has focused its efforts on a better understanding of the Earth-atmosphere system. Awareness of what is occurring will allow not only mitigation of the consequences of human and natural activities, but also improvement of the capability to develop services such as long-term weather and climate forecasting.

A series of programs has been created in order to obtain the required knowledge. The thrust of these programs is the observation of the parameters that govern the Earth radiation budget and global climate change. One generic class of instrument used to accomplish these measurements is the scanning radiometer. A new technology for the

next generation of scanning radiometers for monitoring the Earth radiation budget is presented in this thesis. It is anticipated that this effort will impact NASA's ongoing Cloud and Earth's Radiant Energy System (CERES) program [Wielicki, 1996] and the proposed European Geostationary Earth Radiation Budget (GERB) program.

1.1 The Earth Radiation Budget

Measurement of the Earth radiation budget (ERB) is one approach to quantifying issues such as the greenhouse effect and general climate changes that the Earth-atmosphere system undergoes. The ERB is the difference between the radiation coming from the sun, that is incident to the Earth, P_s (W), and the radiation leaving the Earth into space. The radiation leaving the Earth is composed of shortwave solar radiation reflected from the Earth and its atmosphere, P_r (W), and longwave radiation emitted by the surface and the atmosphere of the Earth, P_e (W). Thus, the hypothesis on the ERB under steady conditions (ERB = 0) may be written symbolically as

$$P_s = P_r + P_e . \tag{1.1}$$

In equilibrium conditions, the radiation absorbed by the Earth and its atmosphere P_a (W) is equal to the net radiation leaving the Earth-atmosphere system,

$$P_a = P_e = P_s - P_r . \tag{1.2}$$

A descriptive model of the global energy balance is illustrated in Figure 1.1. The top of the atmosphere receives an average of 340 W/m^2 from the sun. About thirty percent of this radiation is reflected back into space and then, in order to maintain equilibrium, the Earth re-emits the other 70 percent. When equilibrium is perturbed, for example by the greenhouse effect, the emitted radiation will be affected. Then the Earth will heat up or cool down in order to try to reach a new radiative balance [Wielicki, 1995]. In the case of global heating the increased presence of clouds, which improve the shortwave reflection, would have a cooling effect on the system. In this scenario the question would be: What is the relative size of the warming effects? Is the Earth-

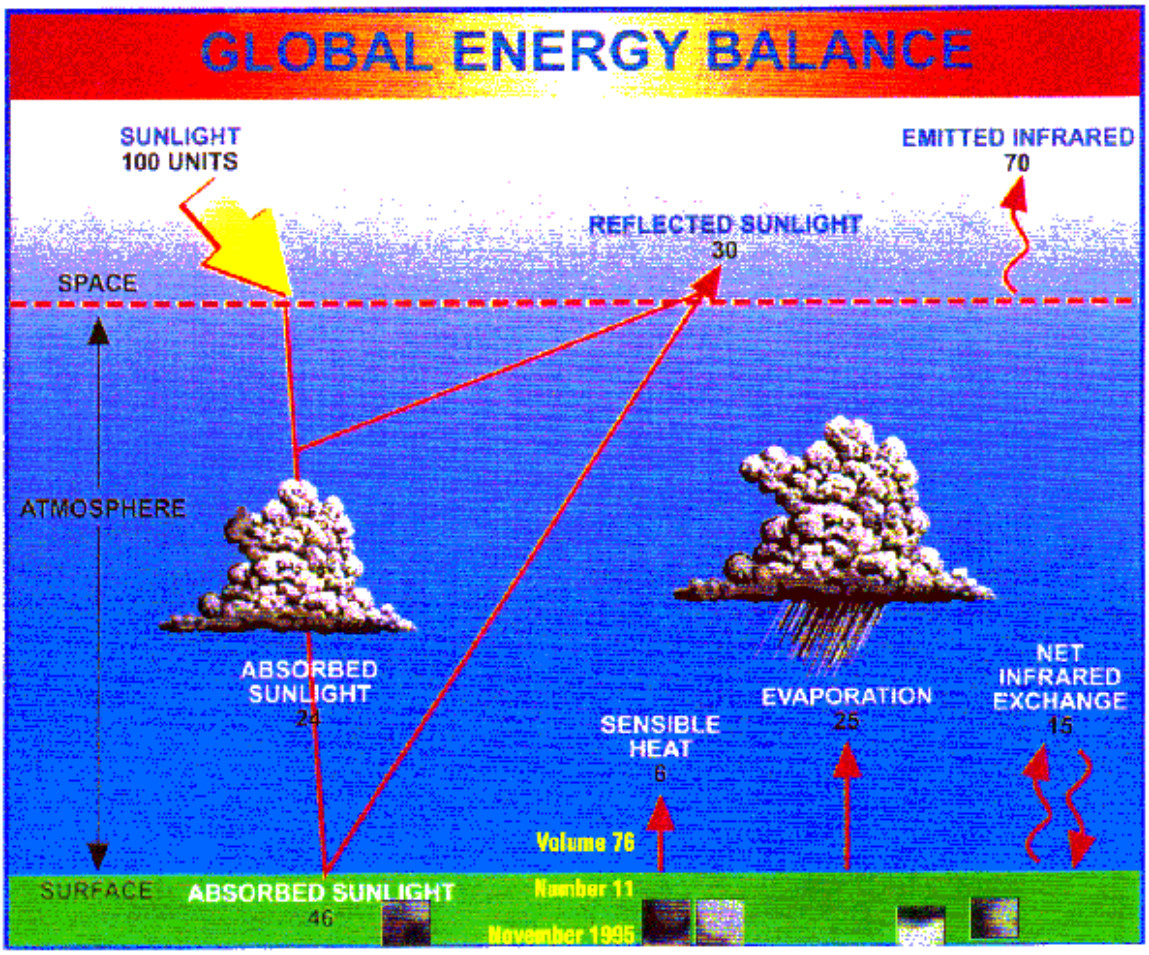

Figure 1.1 Illustration of the global energy balance at the top of the atmosphere and at the surface of the Earth [Bulletin of the American Meteorological Society (cover) Volume 76, 1995]

atmosphere system heating up or cooling down? Unfortunately, the net effect is not yet known, and it is still a topic of ongoing research.

NASA's Earth Observing System (EOS) program consists of a series of flight experiments aimed at obtaining sufficient data to quantify the radiation emission and reflection by the Earth. These data will provide information on the variation of the Earth's climate.

1.2 A Brief History of Earth Radiation Budget Measurements

Before satellite observations of the ERB were possible, a great amount of imagination was used by the scientists of the time to determine the radiation budget components. The following paragraph is based on a discussion by Hunt [1986].

Pouillet obtained an estimate of the solar constant 160 years ago, and Abbot and Fowle made the first attempt to determine the components of the Earth radiation budget at the beginning of this century [Hunt, 1986]. According to Hunt, Very in 1912 and Danjon in 1936 used the ratio of the sunlit to Earth-lit brightnesses of the lunar disk to get values of the Earth's albedo. In the 1940's the advance in laboratory spectroscopic studies provided more complete observations of atmospheric components like water vapor, ozone, and carbon dioxide and by the end of the decade the first space-borne observations of weather were obtained from cameras on sub-orbital rockets.

On February 17, 1959, Explorer 6 took the first satellite picture of the Earth's cloud cover, thereby launching the first of three generations of Earth radiation budget satellite missions between 1959 and 1984 [House, 1986]. In this first generation, satellites such as Explorer 7, TIROS 2, and TIROS 7 had orbital inclination angles reaching mid-latitude regions of the Earth. The principal problem that these satellites faced was their limited or even nonexistent data storage capacities. During the second-generation missions (1960-1981) daily global coverage of the Earth was possible thanks to the power of satellites such as Research/ESSA (1960) Nimbus 3 (April 14 1969) and the NOAA series beginning in December 11, 1970. These satellites also extended the duration of spacecraft measurements to several years. The third generation missions began with the Earth Radiation Budget Experiment (ERBE). The ERBE program was created as an answer to the need for sufficient data to cover the sampling requirements for each component of the ERB: direct solar irradiance, reflected short-wave radiation, and emitted long-wave radiation [Barkstrom, 1986]. The first of the three ERBE satellites was launched from space shuttle *Challenger* (Mission 41-G) on October 5, 1984 [Kopia, 1986]. Additional ERBE instruments were placed in orbit on the National Oceanographic and Atmospheric Administration NOAA-9 satellite, that operated between February 25,

1985, and November 7, 1988, and on the NOAA-10 satellite that operated from December 17, 1986, to September 16, 1991. Presently, NOAA has NOAA-12, launched in May 1991, and NOAA-14, launched in December, 1994, operating in polar orbits that provide visible and infrared radiometer data, radiation measurements, and ozone levels in the atmosphere [Anon., 1996].

Measurements of the interannual variations of the ERB made from sun-synchronous, polar orbiting spacecraft faced the problem of unknown errors resulting from the different equator crossing times of each spacecraft. Using Data from geostationary satellites such as the Geostationary Operational Environmental Satellite (GOES) and the Meteorological Satellite (METEOSTAT), provide a regular sample of the atmospheric diurnal cycle. This information gives a better understanding of the temporal and spatial sampling errors inherent with sun-synchronous, polar-orbiting space-craft and promotes further investigation of spatial scales and meteorological conditions. Currently, the United States is operating GOES-8, launched on April 13, 1994, and GOES-9, launched on May 23, 1995 [Anon., 1996].

In addition to the GOES program, NASA is also presently using data from the Upper Atmosphere Research Program (UARS) [Anon., 1997 *a*], whose principal purpose is to provide information about the upper atmosphere which can lead to a better understanding of the effects of human activity. UARS was launched on September 12, 1991, from the Space Shuttle Discovery (STS-48). Data are collected from a near-circular Earth orbit of about 585 km altitude and 57-deg inclination.

In order to provide a new set of measurements by the end of this century, NASA has planned the Clouds and the Earth's Radiant Energy System (CERES) program as a part of the Earth Observing System (EOS) program to provide continuity with the type of monitoring that ERBE provided [Barkstrom, 1990]. CERES will provide information to improve the understanding of the role of clouds in the radiation budget and the interactions of the ERB with other components of the climate system. Planned EOS and CERES instruments launches are listed in Table 1.1.

Table 1.1. Planned EOS and CERES instrument launches [adapted from Wielicki, 1995].

Satellite	Sponsor	Launch	Measurements
TRMM [1] (CERES)	Japan/US	Nov. 1997	radiative fluxes and cloud properties
EOS-AM [2] (CERES)	US/Japan	June 1998	radiative fluxes and cloud properties
EOS-PM [3] (CERES)	US/ESA [4]	Dec. 2000	radiative fluxes and cloud properties
METOP [5]	EUMETSAT [6]	2000	cloud properties: complements EOS-AM
EOS-ALT [7]	US	2002	active lidar cloud height

[1] Tropical Rainfall Measuring Mission
[2] Earth Observing System-AM (morning equatorial crossing time)
[3] Earth Observing System-PM (afternoon equatorial crossing time)
[4] European Space Agency
[5] Meteorological Operational Satellite
[6] European Meteorological Satellite
[7] Earth Observing System Altimetry Mission

1.3 The Thermopile Linear-Array Thermal Radiation Detector

The thermopile linear-array thermal radiation detector is a new concept developed by Prof. J. R. Mahan of the Department of Mechanical Engineering at Virginia Tech and Mr. L. W. Langley, president of Vatell Corporation [Mahan, 1996]. It is intended for use on the Geostationary Earth Radiation Budget (GERB) experiment. The GERB instrument is to be carried on ESA's Meteosat Second Generation Satellite (MSG), which is expected to be launched in the year 2000 [Anon. *c*, 1997]. The MSG is a geostationary satellite whose rotation on its axis would produce scans of the linear array detector across the disk of the Earth.

Each of the 256 pixels of the linear-array detector consists of the active junction of a two-junction thermopile. The nominal dimension of each pixel is 60 by 60 μm and is separated from its neighbors by a 3-μm gap etched by a laser, as shown in Figure 1.2. Figure 1.3 provides a profile view of a single pixel detector and the disposition of the materials.

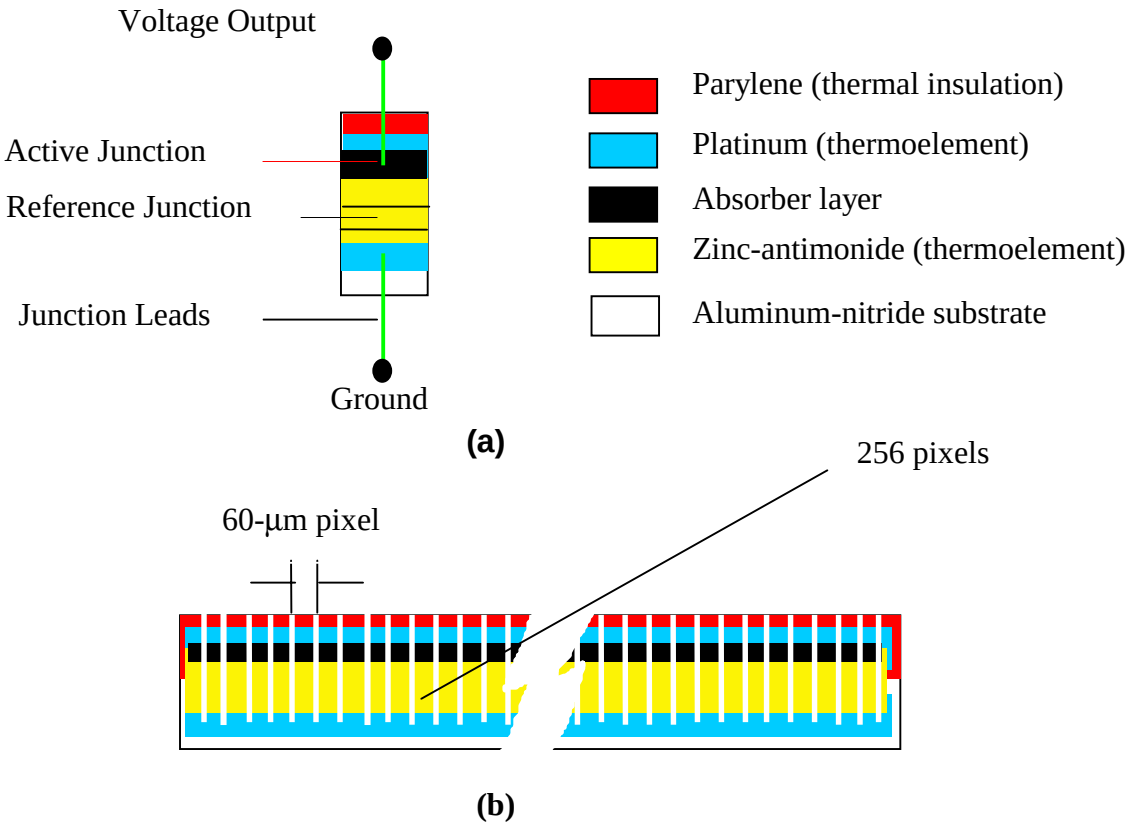

Figure 1.2. (a) Detail of a single pixel and (b) the thermopile linear-array [adapted from Mahan, 1997]

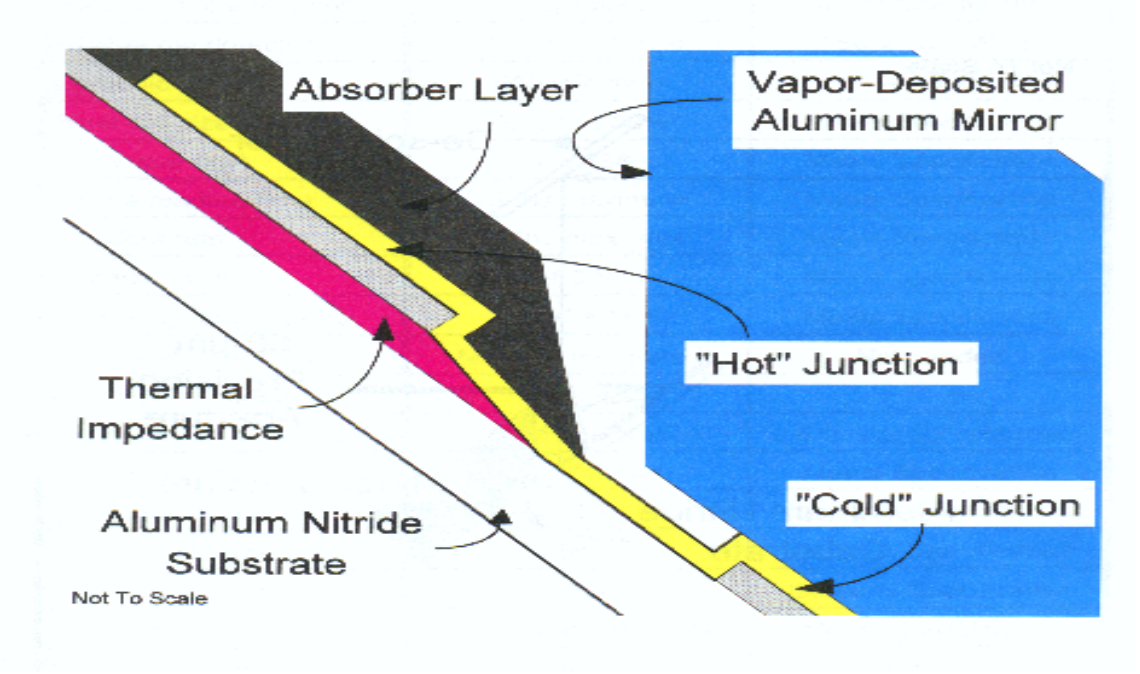

Figure 1.3 Profile view of a single pixel of the thermopile linear-array
[Adapted from Mahan, 1996]

The linear array would be mounted in one wall of a mirrored, wedge-shaped cavity, as shown in Figure 1.4. The incoming radiation enters through the 60-μm slit at the top of the cavity and strikes the exposed active junctions of the thermopile. Weckmann [1997] reports complete documentation of the thermoelectric performance of the thermopiles. The optical performance of the detector and its cavity is investigated in the current thesis.

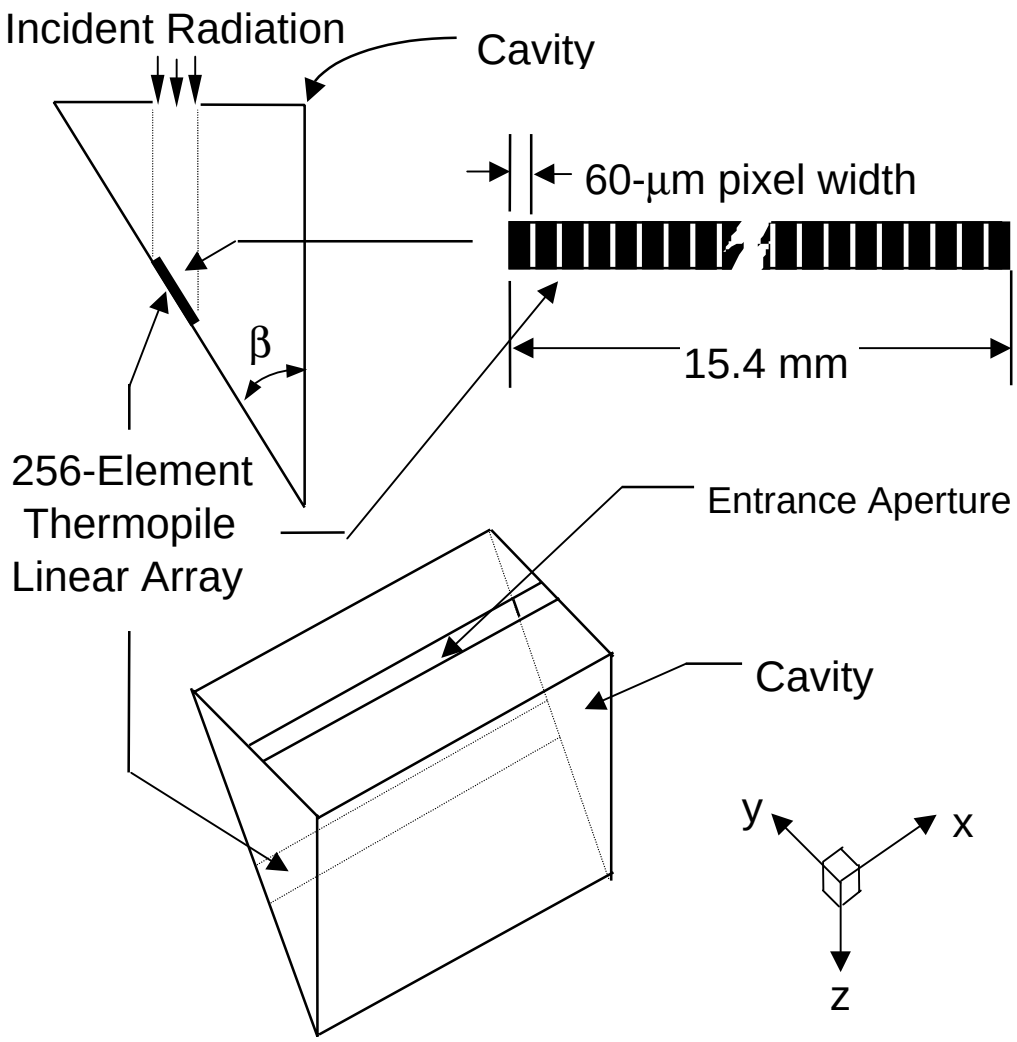

Figure 1.4 The thin-film thermopile linear-array thermal radiation detector concept [Mahan, 1997]

1.4 Motivation and Goals

For the last two years, the Thermal Radiation Group, led by Dr. J. Robert Mahan of the Department of Mechanical Engineering at Virginia Polytechnic Institute and State University, has been working to develop a new technology for thermal-radiation detectors. The principal goal has been to determine the viability of adaptation of these detectors to the next generation of spaceborne ERB radiometers.

In order to attain this objective, numerical models of the detector and the cavity have been developed, and engineering prototypes have been fabricated and used to confirm the behavior predicted using the models.

The principal goal of this thesis is to develop a thermal radiative model for the thermopile linear-array thermal radiation detector using the Monte-Carlo ray-trace (MCRT) method. Since this is a numerical model, all of the dimensional and physical characteristics can be easily changed, a feature which facilitates parametric studies. The model has been implemented in the form of a FORTRAN program and permits calculations of quantities characterizing the optical cross-talk among pixels of the detector and also facilitates the decision-making process relative to optimum design of the detector. The model has the capability to predict the radiation exchange between the surfaces of the cavity and the detector and the radiative noise contributed by the surfaces of the cavity to the detector. In the current thesis the model is used to calculate the fraction of incoming radiation that is absorbed by the pixels of the linear-array detector.

Figure 1.5 shows a paradigm of the process followed in this thesis to achieve the goals listed above. After appropriate research has been completed, the model is developed based on the governing physical principles. In Chapter 2 a description of the Monte-Carlo ray-trace method is presented, as well as the formulation used in this thesis. Then, Chapter 3 gives a complete description of the model and the application of the MCRT method to develop the code. Next, in Chapter 4 the results obtained using the model are presented and a discussion of these results is given. Finally in Chapter 5 some decisions are proposed based on the studies realized in the previous chapter.

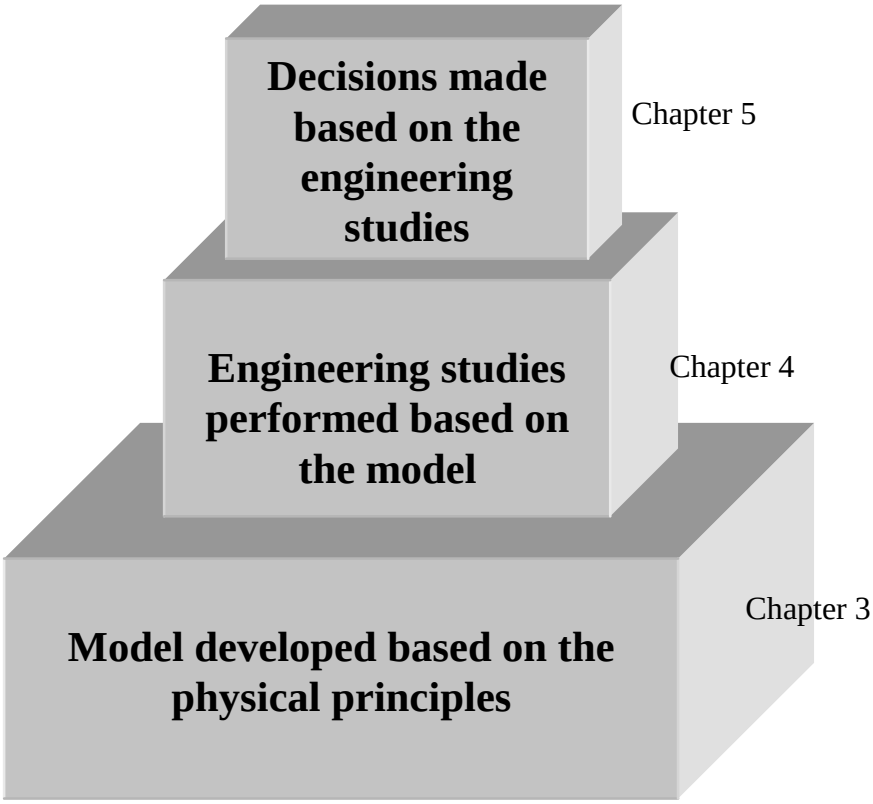

Figure 1.5 Hierarchy of using models to support engineering decisions

Chapter 2. Monte-Carlo Formulation

Many heat transfer problems require the definition of the radiative exchange among surfaces in an enclosure. Even though the formulation of radiation exchange problems is not particularly difficult, it usually leads to tedious integral equations or the algebraic equivalent, a large system of coupled linear algebraic equations. Some simplifying assumptions and approximations usually have to be made in order to resolve the inherent problems. For example, the workload may be reduced tremendously by assuming that the medium filling the cavity does not participate in the radiative exchange and that the surfaces behave only as diffuse and gray emitters, absorbers, and reflectors of radiation. These assumptions lead to the definition of configuration factors that account for the geometrical effects. However, since no surface is purely diffuse, the validity of using configuration factors is limited. In 1962 Seban suggested that the reflectivity of many surfaces of practical engineering interest can be expressed as the sum of a diffuse and a specular component [Sparrow, 1962]. Using this approximation the reflectivity can be written

$$\rho = \rho^d + \rho^s . \tag{2.1}$$

Based on this idea, Mahan and Eskin [1984] introduced the concept of the *distribution factor*. Later, Mahan [1988] defined the *total radiation distribution factor* D_{ij} as "the fraction of the total radiation emitted from surface element i which is absorbed by surface element j, due both to direct radiation and to all possible reflections within the enclosure." This definition includes directional emission and absorption and bidirectional reflection. The model developed in this thesis assumes only diffuse emission and absorption and diffuse-specular reflection and so the *diffuse-specular, total distribution*

factor $D_{ij}^{'}$ is used. This simplifying assumption is justified by the choice of coatings to be used in the fabrication of the proposed detector concept.

2.1 The Diffuse-Specular, Total Distribution Factor

The diffuse-specular, total distribution factor $D_{ij}^{'}$ is defined as the fraction of total thermal radiation (W) emitted diffusely from surface element i that is absorbed by surface element j, due to direct radiation and to all possible diffuse and specular reflections within the enclosure. Using this distribution factor, the radiative energy emitted by surface i, which is absorbed by surface j, may be written as

$$Q_{ij} = \varepsilon_i A_i \sigma T_i^4 D_{ij}^{'} \quad \text{(W)}, \tag{2.2}$$

where ε_i is the hemispherical, total emissivity of surface i, A_i is the area of surface i (m^2), σ is the Stefan-Boltzman constant ($5.6696 \times 10^{-8} Wm^{-2}K^{-4}$), and T (K) is the temperature of surface i. Equation 2.2 may be taken as the definition of $D_{ij}^{'}$. The distribution factor has three useful properties [Mahan, 1998]:

1. Conservation of energy

$$\sum_{j=1}^{n} D_{ij}^{'} = 1.0, \quad 1 \le i \le n, \tag{2.3}$$

2. Reciprocity

$$\varepsilon_i A_i D_{ij}^{'} = \varepsilon_j A_j D_{ij}^{'}, \quad 1 \le i \le n, 1 \le j \le n, \tag{2.4}$$

3. Combination of reciprocity and conservation of energy

$$\sum_{i=1}^{n} \varepsilon_i A_i D_{ij}^{'} = \varepsilon_j A_j, \quad 1 \le j \le n. \tag{2.5}$$

In Equations 2.3, 2.4 and 2.5, n is the number of surface elements into which the cavity has been divided, ε is the hemispherical, total emissivity of a given surface element, and A is its surface area.

The conservation of energy relation and the reciprocity relation may be used to detect and eliminate errors made during the calculation of distribution factors or to find unknown distribution factors from known distribution factors (but not both).

It is noted that it is possible to define other distribution factors; for example, if the enclosure has an opening through which radiation may pass, the opening can be treated as a black membrane that absorbs all incident radiation and that has an equivalent blackbody temperature. Then the distribution factor

$$D'_{oj} = Q_{oj}/Q_o \qquad 1 \le j \le n\,, \tag{2.6}$$

can be defined where Q_o is the power (W) entering through the opening and Q_{oj} is the power (W) entering the enclosure through opening o which is absorbed by surface element j.

The value of the distribution factor does not depend solely on geometry but also on the radiative characteristics of the surfaces making up the cavity. This means that it is not possible to use traditional methods used to find configuration factors to estimate distribution factors. Distribution factors are estimated using the Monte-Carlo ray-trace (MCRT) method.

2.2 The Monte-Carlo Ray-Trace (MCRT) Method

The Monte-Carlo ray-trace (MCRT) method solves radiation heat transfer problems by performing statistical sampling experiments on a computer using random numbers. The method is named after the capital of the principality of Monaco, famous for its casino, because the random numbers could be obtained by dropping a ball in a spinning roulette wheel [Anon, 1997 *b*].

The MCRT method is sometimes described as a statistical approach where a "game", or model, with the same behavior of the physical process being modeled replaces the specific problem, producing the same outcome as the physical process but with the advantage that the "game" is easier to play.

The Thermal Radiation Group at Virginia Polytechnic Institute and State University has been using the MCRT method for many years. Meekins [1990] and

Bongiovi [1993] used the MCRT to model scanning radiometers, Nguyen [1996] used it to characterize the performance of a mirror attenuator mosaic, Walkup [1996] used it to create a radiometric imaging design tool and Turk [1994] developed a reverse MCRT model to predict the infrared image of jet aircraft and plumes, etc.

In this approach radiation energy emitted from a given surface is divided into a large number N_i of discrete and uniform energy bundles. Thus, solving a thermal radiation problem by the MCRT method implies tracing the history of these bundles from their emission by surface element i, through a series of reflections on other surface elements, to their absorption by one of the surface elements j of the enclosure. Using the properties of the enclosure and the laws of probability it is possible to determine the number of energy bundles N_{ij} emitted by surface i and absorbed by surface j. Then the distribution factors may be estimated as

$$D_{ij} \cong \frac{N_{ij}}{N_i}. \tag{2.7}$$

As N_i becomes increasing large, the quality of the estimate increases. In practice the distribution factor D_{ij} can be estimated to an arbitrary degree of accuracy using a finite but large value of N_i.

Once all the properties of the surfaces are defined, the MCRT method can be used to determine the value of the distribution factor. The following development is adapted from Mahan [1998]. The logic flow chart for applying the MCRT method to obtain radiation distribution factors is shown in Figure 2.1. The standard technique is to release a large number of energy bundles from randomly selected locations on a given surface element and then to trace their paths through a series of reflections until they are absorbed by another (or the same) surface element. The number of bundles used depends on the required accuracy and on the availability of computer resources. Normally, 100,000 bundles is considered a minimum number to release from each surface of the enclosure for statistically significant results, with one million being common. The normal steps in

numerical implementation of the MCRT are as described below. The step numbers refer to the block numbers in the logic flow chart.

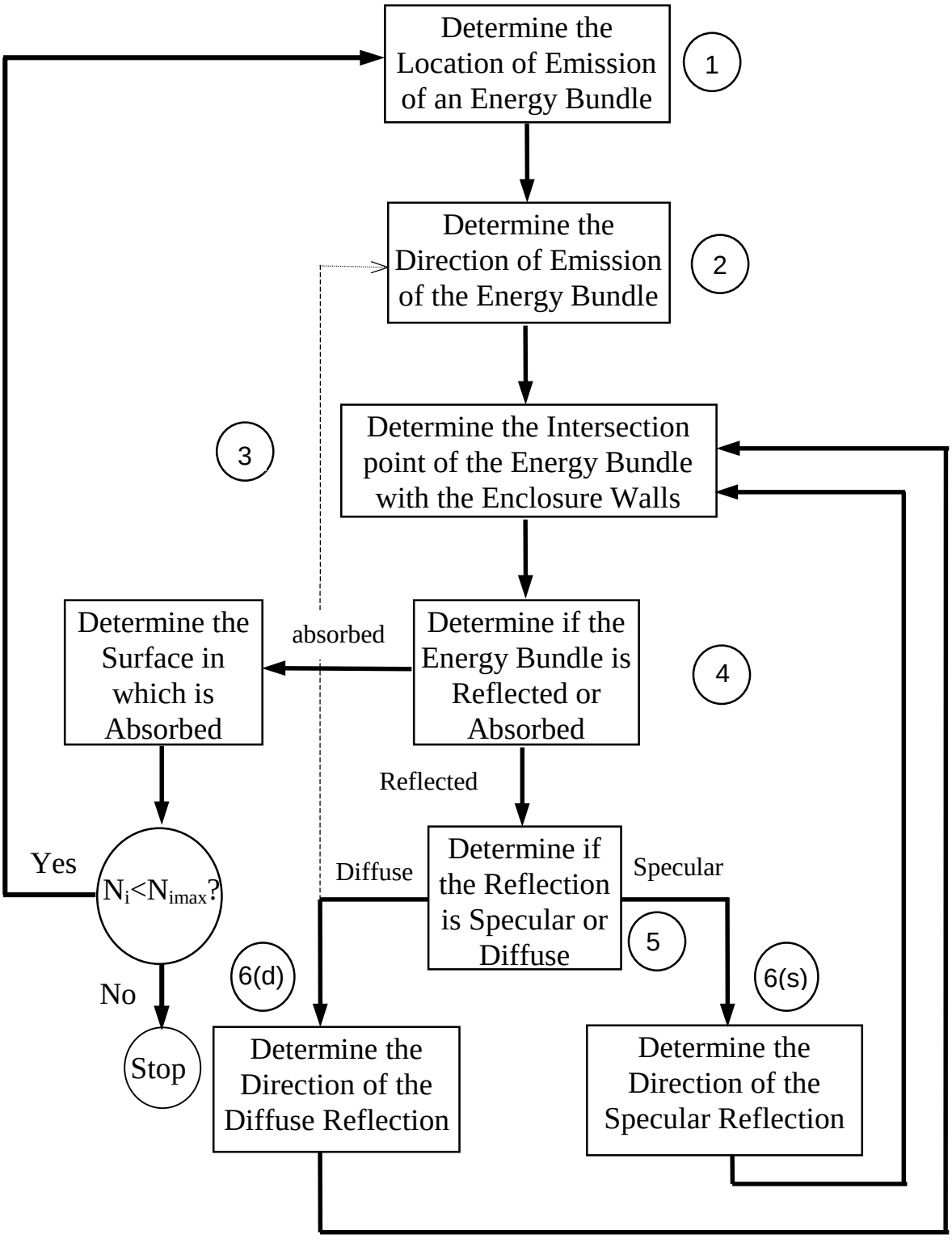

Figure 2.1 Logic diagram for implementing the Monte-Carlo ray-trace method for a given source surface in a diffuse-specular, gray enclosure

1. Determine the location of emission of an energy bundle.

In the problem at hand the energy bundle is not really emitted but rather enters the cavity through an opening, the aperture, as shown in Figure 1.4. A pseudo-random number generator is used to generate a very long sequence, usually tens of millions, of highly uncorrelated random numbers uniformly distributed between zero and unity. Three consecutive numbers, R_x, R_y, R_z, are drawn from a population of generated previously random numbers. Then in the particular case of a planar rectangular surface (the present case), the location of emission is in principle defined by

$$x = x_{min} + (x_{max} - x_{min})R_x, \tag{2.8}$$

$$y = y_{min} + (y_{max} - y_{min})R_y, \tag{2.9}$$

and

$$z = z_{min} + (z_{max} - z_{min})R_z. \tag{2.10}$$

In Equations 2.8 through 2.10, the subscripts *min* and *max* denote, respectively, the minimum and maximum value of the appropriate coordinate on the surface element. Note that in practice only two of these equations are actually needed to determine the coordinates (x,y,z) of the point of "emission" of the energy bundle because the third coordinate can be calculated using the equation of the plane,

$$n_x(x - x_0) + n_y(y - y_0) + n_z(z - z_0) = 0. \tag{2.11}$$

In Equation 2.11, n_x, n_y, and n_z are the coordinates of the unit normal vector to the plane and x_0, y_0, and z_0 are the coordinates of any point on the surface.

2. Determine the direction of emission of the energy bundle.

Howell [1992] gives expressions for the direction of diffuse emission as a function of two independent coordinates: the circumferential angle ϕ in the plane of the

surface with respect to a local unit surface tangent $\vec{t}$, and the azimuth angle θ with respect to the local unit surface normal $\vec{n}$. These two angles are given by

$$\phi = 2\pi R_{\phi} \tag{2.12}$$

and

$$\theta = \sin^{-1}\sqrt{R_{\theta}}\ , \tag{2.13}$$

where R_{ϕ} and R_{θ} are two random numbers uniformly distributed from zero and unity. The angles ϕ and θ and the normal and tangent vectors are used together to determine the direction cosines (l, m, n) of the path along which the emitted energy bundle travels. The direction cosines are defined as

$$l = \cos\alpha, \tag{2.14}$$

$$m = \cos\beta, \tag{2.15}$$

and

$$n = \cos\gamma, \tag{2.16}$$

where α, β, and γ are the angles that a directed line makes with respect to the coordinates x, y, and z, respectively, as shown in the Figure 2.2. Angles ϕ and θ are defined with respect to the local coordinates $(\vec{t},\ \vec{n})$, which must be transformed to global coordinates (x, y, z). The relation between the local and global coordinates is shown in Figure 2.3. Vectorial manipulation and/or coordinate transformation are required to relate $(\vec{t},\ \vec{n})$ and $(x,\ y,\ z)$, and thus the angles ϕ and θ to the direction cosines (l, m, n).

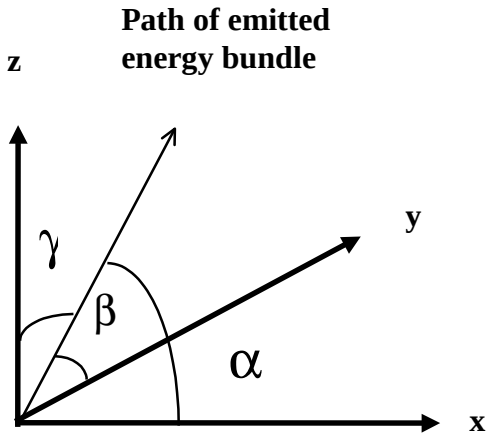

Figure 2.2 Illustration of the direction cosines

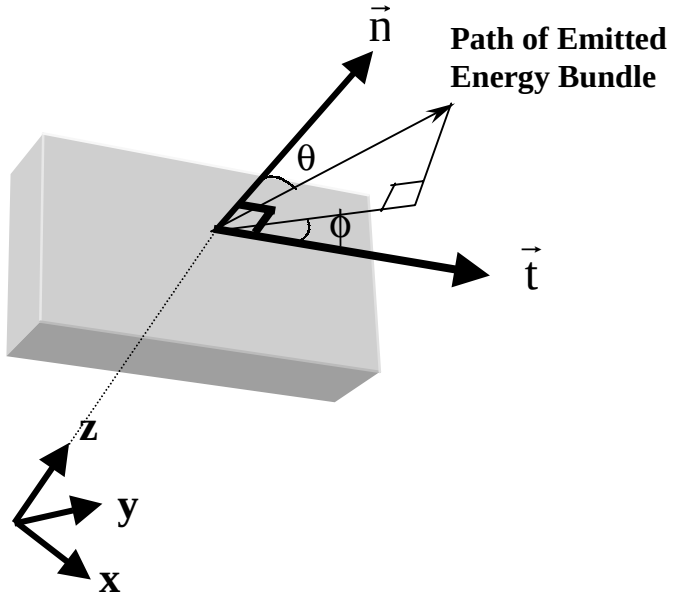

Figure 2.3 Relationship between the local and global coordinates

In the case of radiation entering the GERB cavity through the slit (see Figure 1.4), the values of the direction cosines are assumed to be l = 0, m = 0, and n = 1.

3. Determine the point of intersection of the emitted energy bundle with the enclosure walls.

Using the equations of the surfaces in the cavity and the equations of the line for the path along which the energy bundle travels, all the possible points of intersection of the bundle with the walls can be found. Since the equations of a line describe an infinitely long line and, in the case of the current study, the equations of the surfaces describe planes infinite in extent, many candidate points of interaction will generally be found. Therefore it is necessary to eliminate all of the points of intersection except the one corresponding to the actual intersection of the path of the energy bundle and the cavity wall. This problem is illustrated in Figure 2.4.

In the situation depicted in Figure 2.4, an energy bundle is emitted from Point a in the direction of Point b. The equations of the line are given by

$$T = \frac{x - x_a}{l} = \frac{y - y_a}{m} = \frac{z - z_a}{n}, \tag{2.17}$$

where T is the length of the line connecting x_a, y_a, z_a with x, y, z. Equations 2.17 and the equation of each surface of the enclosure constitute sets of four equations in the four unknowns x, y, z, and T. In the example of Figure 2.4 when Equations 2.17 are solved with the equations of the surfaces, four points are obtained: a, b, c, d. From the figure, it is clear that Point b is the desired point. However, ensuring that the computer "selects" the correct point is a task accomplished through the following three-step process:

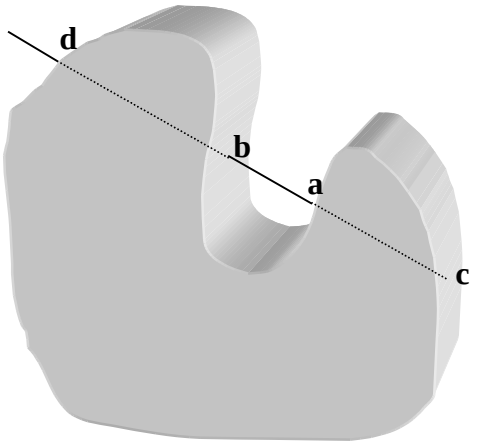

Figure 2.4 Intersections of a straight line with the surfaces of an arbitrary enclosure

1. First, eliminate the point of origin (Point a). This point will always emerge as a candidate. One way to do this is to compare the coordinates of the origin point with the coordinates of the source of emission. If these coordinates are the same, within some specified tolerance, this point is rejected.
2. Next, eliminate the "back" candidate (Point c). This may be accomplished by forming the dot product of the inward-directed surface normal with the vector

$$(x_c - x_a)\vec{i} + (y_c - y_a)\vec{j} + (z_c - z_a)\vec{k}$$

   directed from the source point toward the candidate point. A positive value of this dot product indicates that the candidate lies in front of the source, while a negative value indicates that the candidate lies behind the source and therefore must be rejected.
3. Finally, choose the nearest candidate from among all the candidates that lie in front of the source. In order to do this, it is necessary to compare the distances from the source to all the candidates in front of it, and then to choose the shortest one. The distance T between any two points is given by Equations 2.17.

Equations 2.17 may be written in the form

$$x = x_a + lT, \tag{2.18}$$

$$y = y_a + mT, \tag{2.19}$$

and

$$z = z_a + nT. \tag{2.20}$$

The form of Equations 2.18 through 2.20 avoids the possible division by zero that could occur if one or two of the direction cosines have values of zero (whenever the path of an energy bundle is normal to a given coordinate axis).

4. Determine whether the energy bundle is absorbed or reflected.

Using the assumption that all surfaces are diffuse-specular, gray reflectors, it is possible to write that

$$\alpha = 1 - \rho = 1 - \rho^d - \rho^s, \tag{2.21}$$

where ρ^d is the diffuse component of reflectivity and ρ^s is the specular component.

The absorptivity may be interpreted as the probability that an incident energy bundle will be absorbed. Then each time that an energy bundle intercepts a surface, the next available random number R_α, uniformly distributed between zero and unity, is drawn and compared with the absorptivity. If the random number is less than or equal to the absorptivity, the energy bundle is absorbed; otherwise, it is reflected. If the energy bundle is absorbed, the value of N_{ij} is incremented and the MCRT method returns to Step 1 with the emission of a new energy bundle. If the energy bundle is reflected, the logic continues to the next step.

5. Determine if the reflection is diffuse or specular

The *specularity ratio* r_s is a surface property, defined as the ratio of the specular component of reflectivity to the reflectivity,

$$r_s = \frac{\rho^s}{\rho} = \frac{\rho^s}{\rho^s + \rho^d}. \tag{2.22}$$

This ratio can be interpreted as the probability that a reflection from the surface in question is specular. A random number R_s, uniformly distributed between zero and unity is drawn and compared with r_s. If R_s is less than or equal to r_s, the reflection is specular; otherwise it is diffuse. If the reflection is specular, the logic branches to Step 6(s), whereas if the reflection is diffuse, the logic branches to Step 6(d).

6(s) Determine the direction of the specular reflection.

A reflection is said to be specular when the paths of the incident and reflected energy bundles and the surface normal all lie in the same plane, and the angle between the reflected energy bundle and the surface normal is equal to the angle between the incident energy bundle and the surface normal. These relationships are illustrated in Figure 2.5. The rules illustrated in this figure may be combined to yield

$$\vec{V}_r = \vec{V}_i - 2(\vec{V}_i \cdot \vec{n})\vec{n} = \vec{V}_i + 2\left|\vec{V}_i\right|\cos\theta\,\vec{n} \tag{2.23}$$

where

$$\vec{V}_i = (x_b - x_a)\vec{i} + (y_b - y_a)\vec{j} + (z_b - z_a)\vec{k}. \tag{2.24}$$

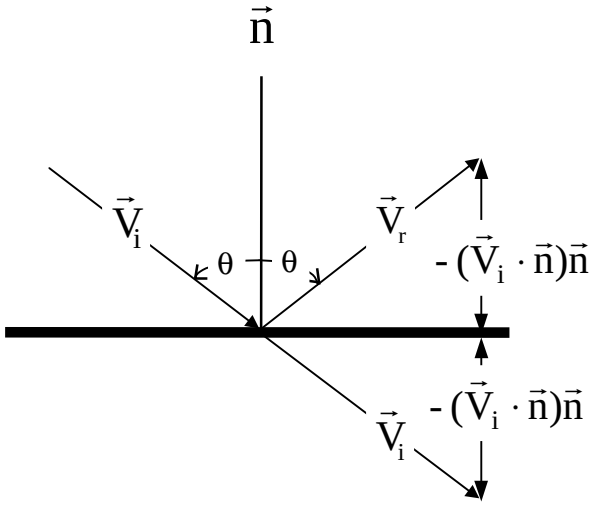

Figure 2.5 Relationship between incident and specularly reflected rays

In Equation 2.24, (x_b, y_b, z_b) are the coordinates of the point where the energy bundle intersects the receiving surface and (x_a, y_a, z_a) are the coordinates of the source point.

The result given by Equation 2.23 may be interpreted in terms of the direction cosines. Knowing that the reflected vector is given by

$$T_r = \sqrt{(V_{r,x})^2 + (V_{r,y})^2 + (V_{r,z})^2}\,, \tag{2.25}$$

then

$$l_r = \frac{V_{r,x}}{T_r}\,, \tag{2.26}$$

$$m_r = \frac{V_{r,y}}{T_r}\,, \tag{2.27}$$

and

$$n_r = \frac{V_{r,z}}{T_r}\,. \tag{2.25}$$

6(d) Determine the direction of the diffuse reflection.

When an energy bundle is reflected diffusely, it retains no knowledge of its history before suffering the reflection. That is, the energy bundle has been reborn as a newly emitted energy bundle. This means that a diffuse reflection is exactly like a diffuse emission. Then the current logic step would be identical to Step 2, as the dashed line in the block diagram of Figure 2.1 indicates.

The steps described above are repeated for a large number of energy bundles, leading to as a final result the distribution factor estimated by

$$D_{ij} \cong \frac{N_{ij}}{N_i}, \tag{2.29}$$

where N_{ij} is the number of energy bundles emitted by surface i and absorbed by surface j, and N_i is the total number of energy bundles emitted by surface i.

Chapter 3. The GERB Detector Model

The thermal radiation detector concept of the GERB instrument and its cavity are shown in Figures 1.2 through 1.4. All of the walls of the cavity are intended to have a high specularity ratio and a low absortivity. The slit is modeled as a membrane that emits collimated radiation into the cavity toward the linear-array detector and absorbs all energy bundles incident to it from the interior. The sensing junction, which is intended to have a high absorptivity and specularity ratio, will consist of a black absorber layer such as CHEMGLAZE 306-Z. Figure 3.1 shows the spectral characterization of several black coatings that were proposed to be used in CERES thermistor bolometer radiometers. These are also potential candidates for the GERB detector.

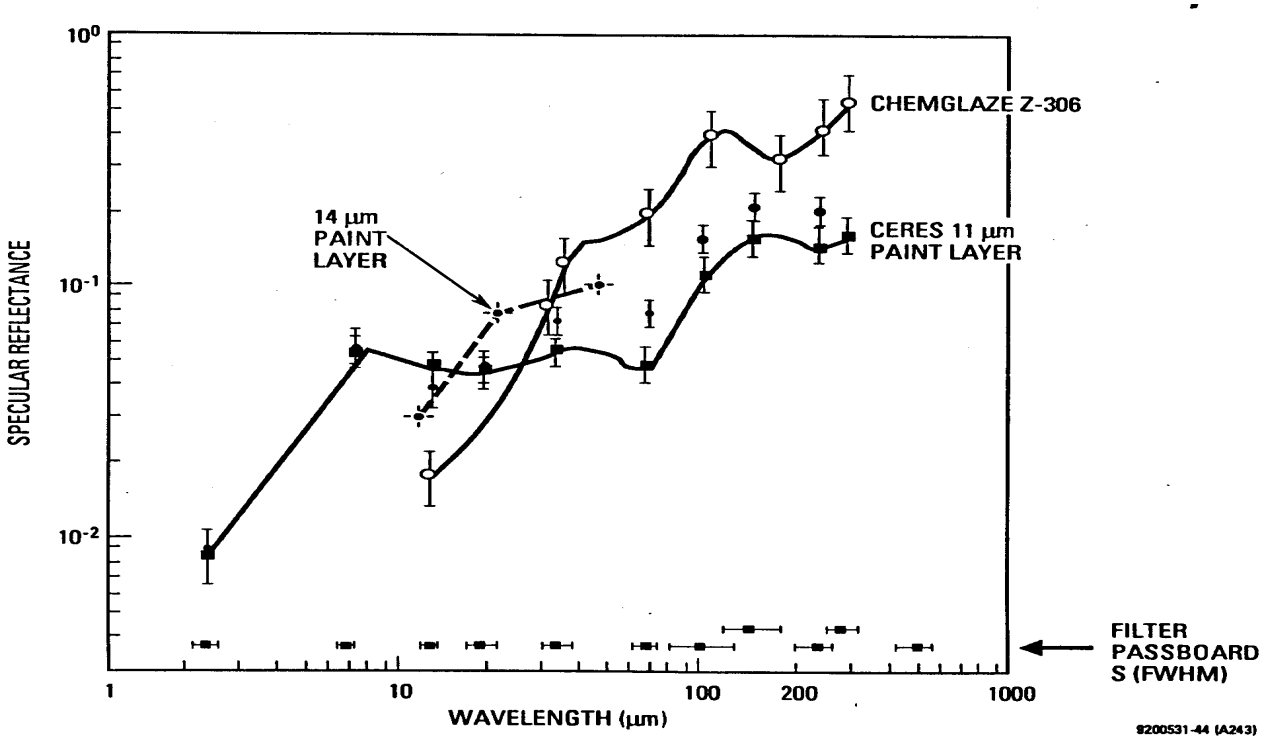

Fig 3.1 Measured spectral flatness of several black coatings [CERES, 1992]

Note that the materials have low reflectivity in the GERB spectral range (0.3 μm to 40 μm) and that the reflectivity is mostly specular. Since the values for the specular reflectivities are specified for any wavelength, Figure 3.1 allows the model to develop a monochromatic analysis. Unfortunately, as shown in the Figure 3.2, real coatings are not spectrally flat, which means that their absorptivities change with the wavelength. However spectral flatness is an important requirement for the GERB detector concept. Table 3.1 gives the specifications for spectral flatness in GERB.

The multiple reflections, which occur between the absorber layer and the mirrored surfaces, produce a "cavity effect" that greatly increases the effective absorptivity in the detector. A general procedure for evaluating the cavity effect is to compare the actual energy emitted from a cavity with that leaving a black-walled cavity [Sparrow, 1966]. In Figure 3.2 the apparent emissivity is plotted as a function of the surface-opening angle 2ϕ for a V-groove cavity. For each value of actual wall emissivity, results are given for wall reflectances that are purely specular and purely diffuse[1]. In both cases the apparent emissivity increases as the opening angle becomes smaller. At the other limit, when the opening angle approaches 180 deg, the apparent emissivity approaches the surface emissivity. Figure 3.3 is a representation of the flattening effect produced for a cavity.

Table 3.1 GERB specifications for spectral flatness

Wavelength Interval	**Percent Change**
0.32 to 10 μm	1.5
10 to 20 μm	5
20 to 40 μm	10

[1]Recall that for gray radiation the emissivity is equal to the absorptivity

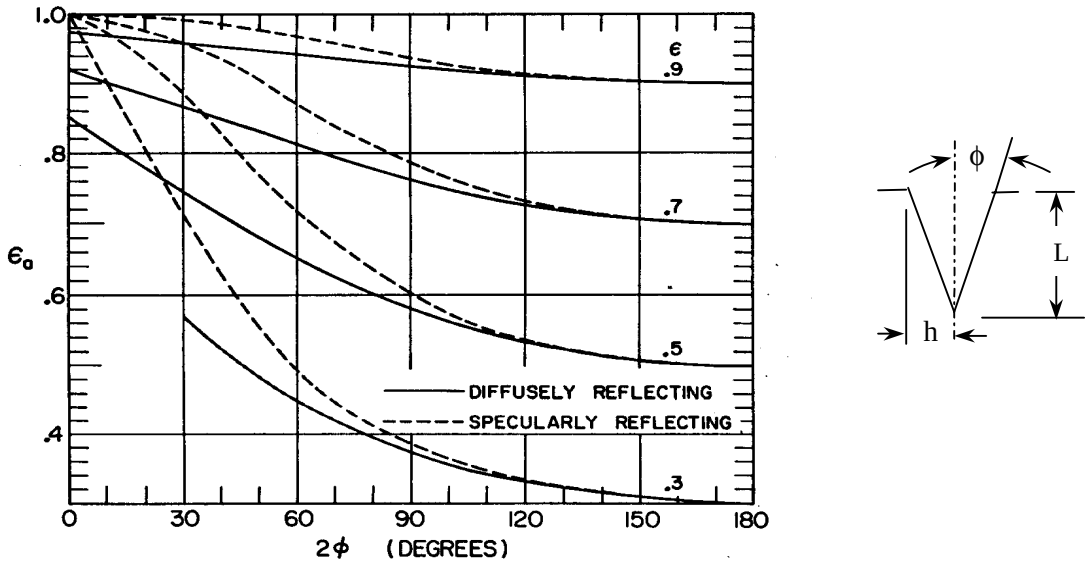

Figure 3.2 Apparent emissivity results for diffusely and specularly reflecting V-groove cavities [Sparrow, 1966].

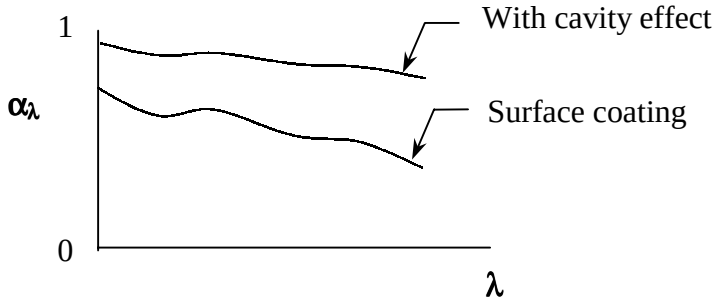

Figure 3.3 Hypothetical case of cavity flattening of spectral response

3.1 Application of the Monte-Carlo Ray-Trace Method

The MCRT method is used here to compose an optical model of the detector and the cavity of the proposed GERB instrument shown in Figures 1.2 through 1.4. The cavity is divided into nine surfaces composed purely of planes, as shown in Figure 3.4.

The detector array (Surface 1) is subdivided in 256 pixels of equal dimension as indicated in Figure 1.4. Except for the detector and the slit (Surface 6), all the walls are assumed to be mirror-like reflectors but with a nonzero absorptivity.

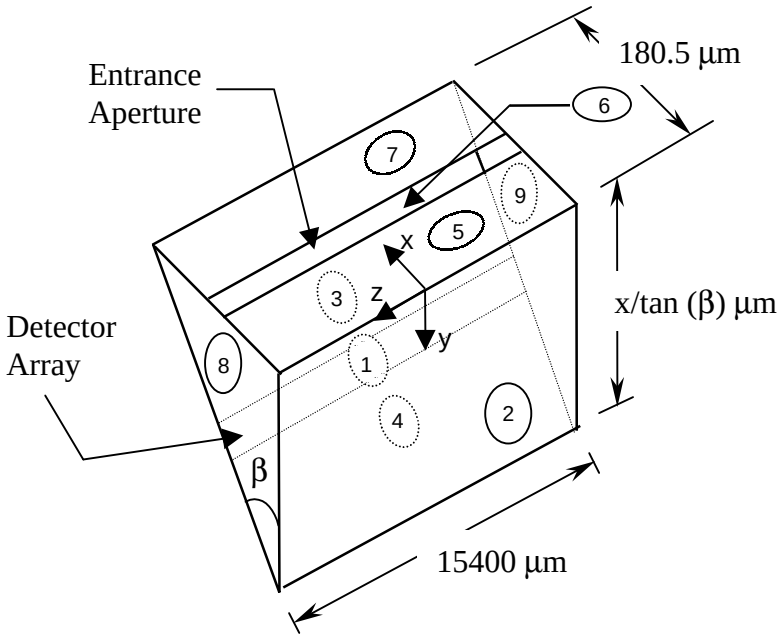

Figure 3.4 Division of the cavity in surfaces

A FORTRAN program, named GERB and listed in the Appendix A, has been written in order to trace all of the energy bundles that enter the cavity. All the dimensions are specified internal to the program with reference to the maximum and minimum values of the surfaces in each coordinate. The program has the capability of simulating the emission of collimated energy bundles from Surface 6 (the entrance slit) and following them until they are absorbed by a surface of the enclosure or escape through the slit. With minor modifications, the number of energy bundles absorbed in each surface and the distribution factors between any pair of surfaces can also be calculated. The program also can be used to perform parametric studies by changing the angle β between Surfaces 2 and 4 or the dimensions of any surface. In order to optimize the design, the properties of the materials can also be changed inside Subroutine PROPERTIES of Program GERB.

At this point it is appropriate to discuss optical limitations of the MCRT method imposed by the effects of diffraction. Since the model deals with simulation of energy bundles treated as rays, the possible presence of diffraction in the problem is a concern. It is well known that the diffraction phenomenon is closely related to the relative size of a

characteristic dimension, L, of an enclosure and the wavelength, λ, of the radiation. In the geometry considered in this thesis, the relation λ/L increases as the energy bundle approaches a corner or an edge (e.g. the angle β and the edge of the slit). These geometric features are illustrated in Figure 3.3. This raises the concern that the underlying assumption of ray-like behavior may not be valid everywhere in the problem domain.

Unfortunately the limit where the MCRT model is no longer valid is currently unknown but is surely geometry dependent. Therefore all the studies realized in this thesis have been done making the assumption that the MCRT method can be applied over the entire geometry. Further studies are currently underway in the Thermal Radiation Group to resolve this question.

In the next chapter the results for the optical behavior of the GERB thermal radiation detector, as well as a statistical evaluation of the model itself, are presented.

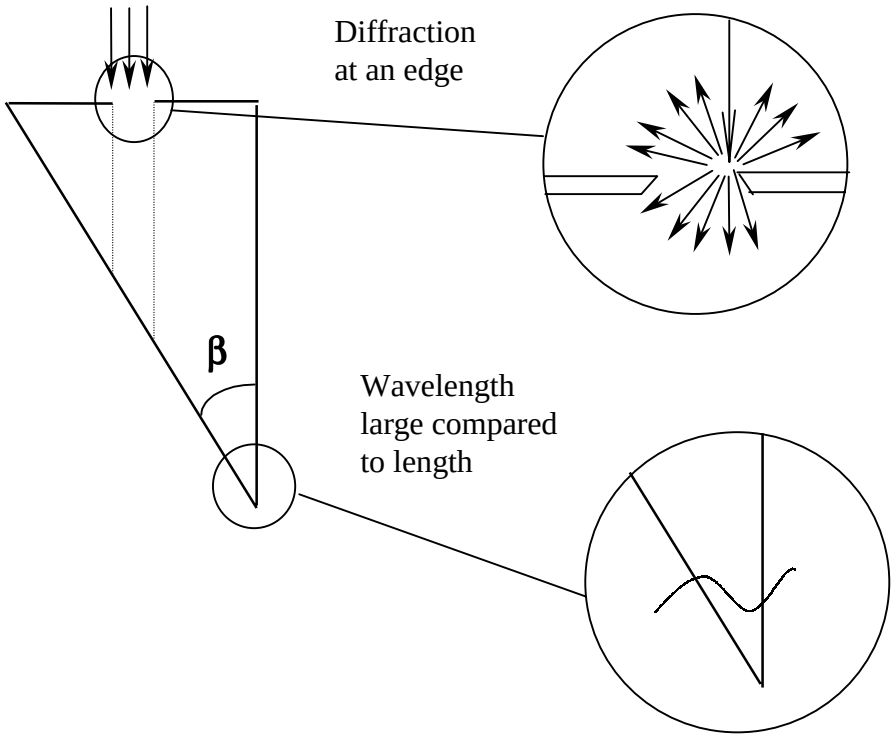

Fig 3.5 Geometric features where diffraction effects are important

Chapter 4. Results and Discussion

This chapter is divided into two major sections. The first section describes a study of convergence and a statistical analysis of the accuracy of the model. Then the second section describes the engineering results obtained from the application of the code. The results are grouped in subsections according to the analysis being conducted. Each subsection describes the way that the program had to be modified to obtain the results, the reasons for running the particular analysis, the results obtained from the program, and a critical discussion of the results.

4.1 Model Testing

The code has been run with up to 100 million energy bundles entering the cavity through the entrance slit in order to determine the distribution factor $D_{6,1}$ (the fraction of energy bundles emitted from Surface 6 that are absorbed in Surface 1). Figure 4.1 shows the convergence of the value for the distribution factor $D_{6,1}$ for the case of a 45-deg wedge angle. Similar results can be demonstrated for other wedge angles. In this figure it is possible to see that the distribution factor estimate begins to converge to an acceptable accuracy when one million energy bundles have been emitted. Most of the cases studied in this thesis were conducted based on the emission of one million of energy bundles.

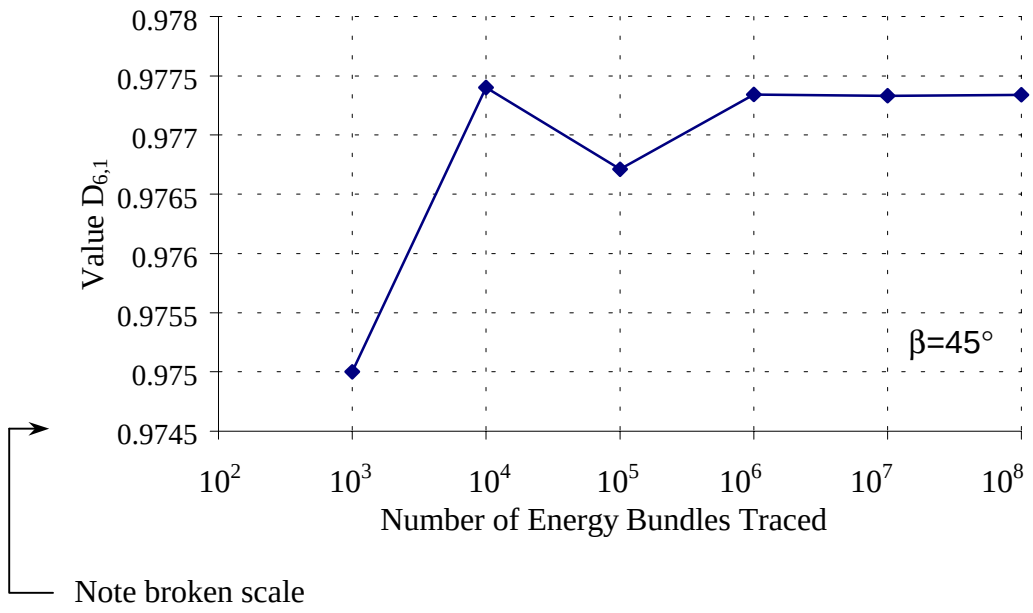

Fig 4.1 Convergence of the distribution factor $D_{6,1}$

The first test used for validation of the code was performed illuminating the two pixels in the middle of the linear array (pixels number 128 and 129) by direct radiation and testing the distribution of the rays absorbed along the detector array. Since the model has a probabilistic basis, it is expected that the distribution of the absorbed rays around the center of the detector will be symmetric. In order to verify that the code is in accordance with this expectation, the statistical technique of hypothesis testing was used. The structure of this technique is formulated with the use of a null hypothesis denoted by H_0 that refers to any hypothesis under test and an alternative hypothesis denoted by H_1, which will be accepted in the case that H_0 is rejected. The basis of this test is the Student's t-test from statistics. Rejection of H_0 at significance level α, which is the maximum probability of rejecting H_0 when it is in fact true, results when t, given by

$$t = \frac{\overline{X} - \mu}{s/\sqrt{n}}, \tag{4.1}$$

is greater than or equal to a critical value based on the t-distribution. More information about the t-test can be found in Koopman [1987], Walpole [1997], and Mahan [1998].

In this special case, the values of $\overline{X}$ and s in Equation 4.1 are given by

$$\overline{X} = \frac{1}{n}\sum_{i=1}^{n}\left(\frac{N_l - N_r}{N_{total}}\right)_i \tag{4.2}$$

and

$$s = \sqrt{\frac{1}{n-1}\sum_{i=1}^{n}\left(\frac{N_l - N_r}{N_{total}}\right)_i^2}, \tag{4.3}$$

where n is the number of pixels (128), N_l is the number of energy bundles absorbed by the pixel i to the left of the center, N_r is the number of energy bundles absorbed by the pixel i to the right of the center, and N_{total} is the total number of energy bundles absorbed by the detector. The hypothesis under test and the alternative hypothesis used in this test are

$$H_0: \quad \mu = 0 \tag{4.4}$$

and

$$H_1: \quad \mu \neq 0. \tag{4.5}$$

From the table for critical values of the t-distribution (available in standard statistical texts such as Hogg [1987], Koopman [1987], or Walpole [1997]), the hypothesis must be rejected if $t > 1.645$ for a level of significance of 0.05.

The results of this analysis for different values of the wedge angle β are presented in the Table 4.1 Note that all the values of t are less than 1.645, which means that the results for the angles tested pass the t-test; that is H_0 is accepted. Thus we conclude that, to a 5 percent level of significance, the distribution of energy bundles about the center of the array is symmetrical, i.e., that the model is unbiased. The values of t for the angles tested are plotted against angle in Figure 4.2. In this graph it is clear that the wedge angle presenting the best symmetry is 45 deg. This is felt to be because the total number of

energy bundles absorbed by the linear-array detector, and thus the sampling, is maximized for this angle.

Table 4.1 Values used in the t-test

Wedge angle β	Sample mean $\overline{X}$	Sample standard deviation s	Total number of energy bundles absorbed by the detector	$\lvert t \rvert$
30	1.36×10^{-5}	3.78×10^{-4}	55655	0.406
40	3.99×10^{-5}	5.51×10^{-4}	59038	0.816
45	1.1×10^{-6}	4.83×10^{-5}	78855	0.255
50	-2.45×10^{-5}	2.08×10^{-4}	56957	1.333
60	8.68×10^{-5}	6.86×10^{-4}	37980	1.427

Figure 4.2 Values of the t statistic for different wedge angles β

4.2 Model Application

In order to make more understandable the reading of the analysis of the results, it is convenient to explain some of the terminology used in this section. In several cases, the discussion of some results is going to refer to vertical or horizontal divisions of any surface, generally Surfaces 1, 3, and 4. The sense of this terminology is illustrated in Figure 4.3.

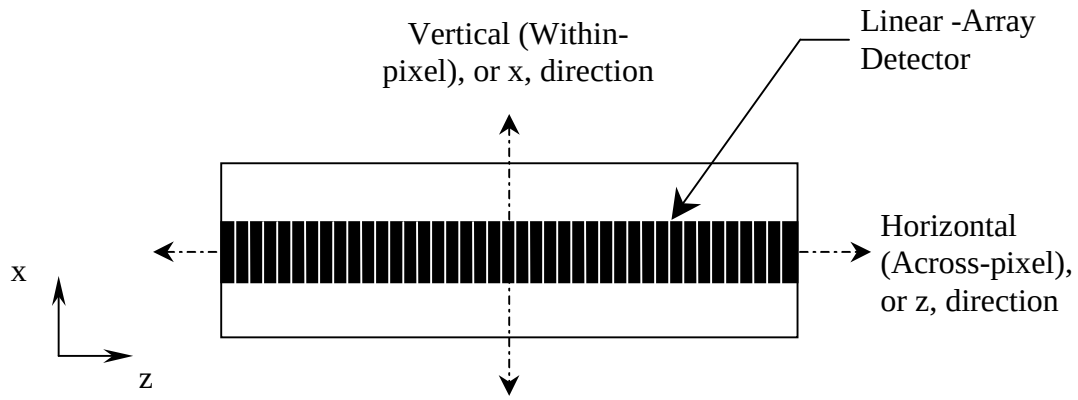

Figure 4.3 Schematic representation of the linear-array thermal radiation detector illustrating terminology

4.2.1 Variation of the Wedge Angle β

One of the principal goals of this thesis is to use the MCRT program described in Chapter 2 to study the behavior of the energy bundles inside the cavities when the value of the wedge angle β varies. First, the program was executed varying the value of the variable DANG from 30 deg to 60 deg in increments of 10 deg. Only the two pixels in the middle were exposed to direct radiation of one million energy bundles (500,000 each). Figures 4.4 through 4.8 show the results of this execution. The scattergrams in Figures 4.4, 4.5, 4.6, 4.7, and 4.8 show the x and z locations where the energy bundles were absorbed by Surfaces 1 (detector), 3, and 4. Note that the scale of the two axes is not the

same. Remember that this plane (Surfaces1, 3, and 4 together) has dimensions of 15400 μm by 180.5 μm. Through study of these figures, it is possible to discern a significant transition in the distribution of the energy bundles absorbed in the thermal radiation detector between β = 40 deg and β = 50 deg. Note that when β = 40 (Figure 4.5) deg more energy bundles seem to be absorbed near the bottom of the detector and when β = 50 deg (Figure 4.7) it seems that more energy bundles are absorbed near the top of the detector. As a result, the program was executed with β = 45 deg (Figure 4.6).

It is possible to see that when β = 45 deg the distribution appears to be more homogeneous in the x-direction but that this also seems to be the case where the most spreading in the z-direction is noted. Further studies are described elsewhere in this thesis to explain this behavior. The most notable characteristic of this set of figures is the distribution of the absorbed energy bundles along the x coordinate as β is changed. This characteristic is referred to here as the taper effect.

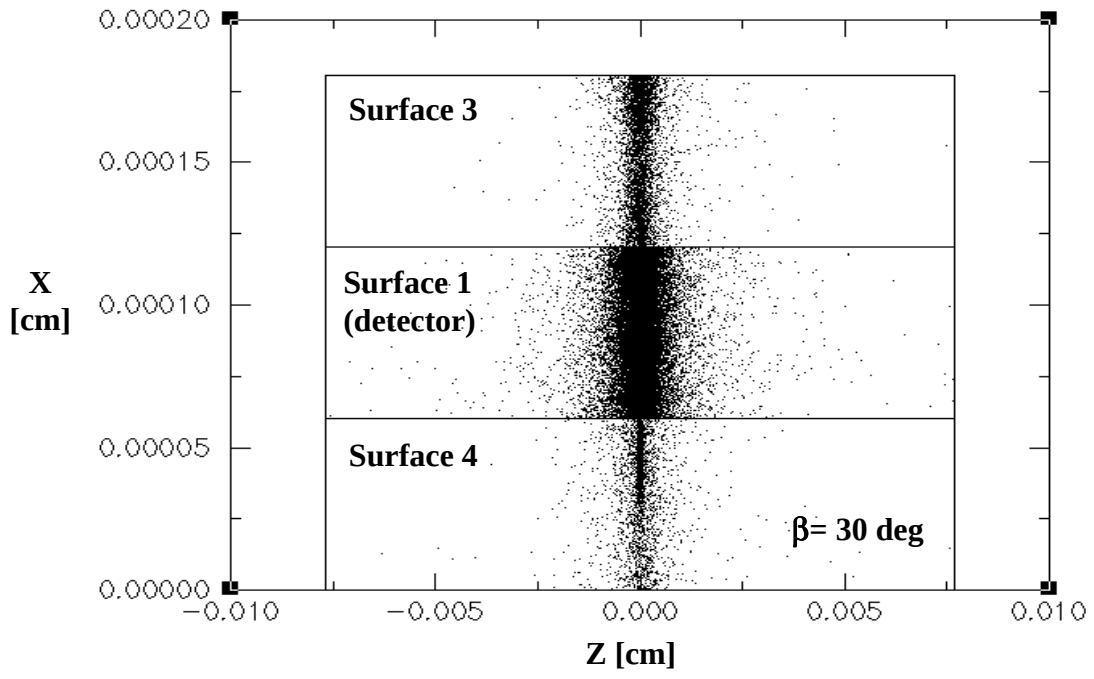

Figure 4.4 Scattergram of energy bundles absorbed by Surfaces 1, 3, and 4 for a wedge angle of 30 deg (nominal values surface optical properties)

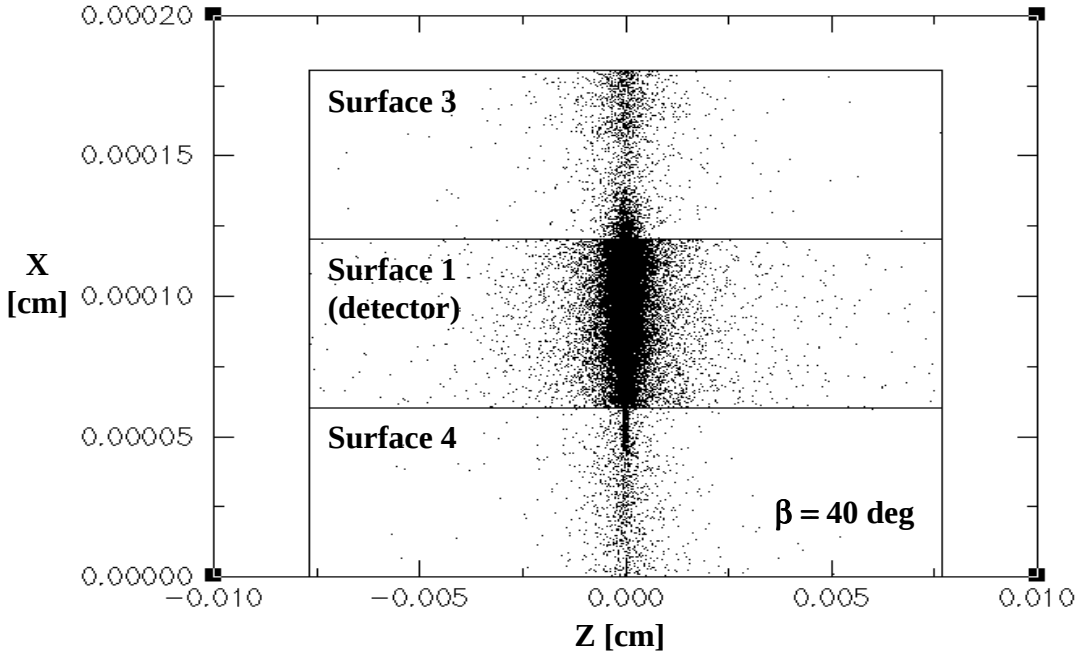

Figure 4.5 Scattergram of energy bundles absorbed by Surfaces 1, 3, and 4 for a wedge angle of 40 deg (nominal values surface optical properties)

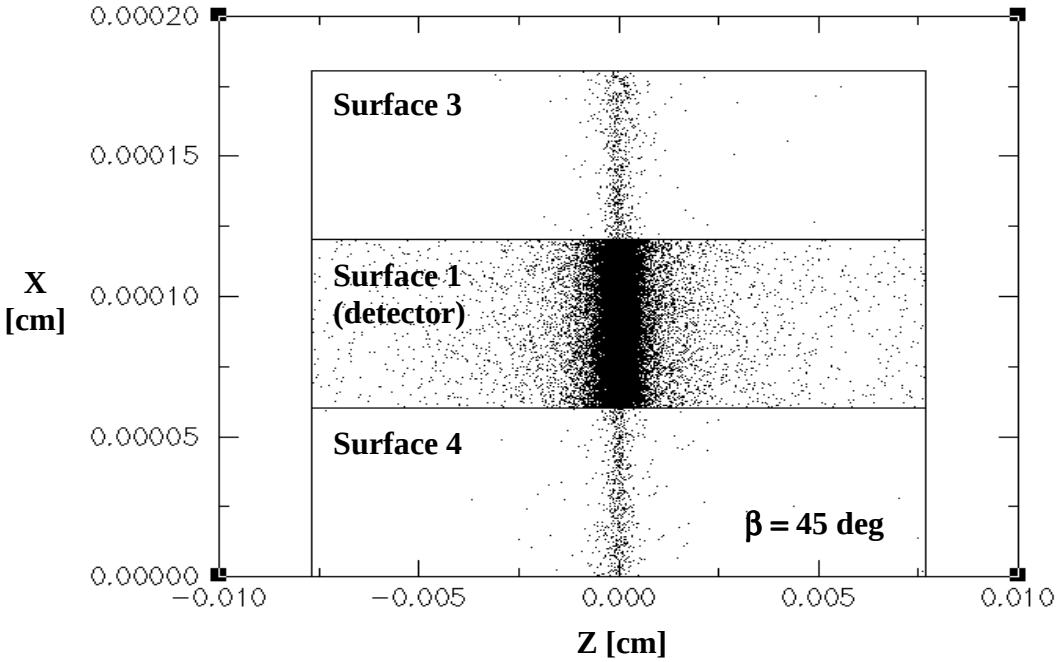

Figure 4.6 Scattergram of energy bundles absorbed by Surfaces 1, 3, and 4 for a wedge angle of 45 deg (nominal values surface optical properties)

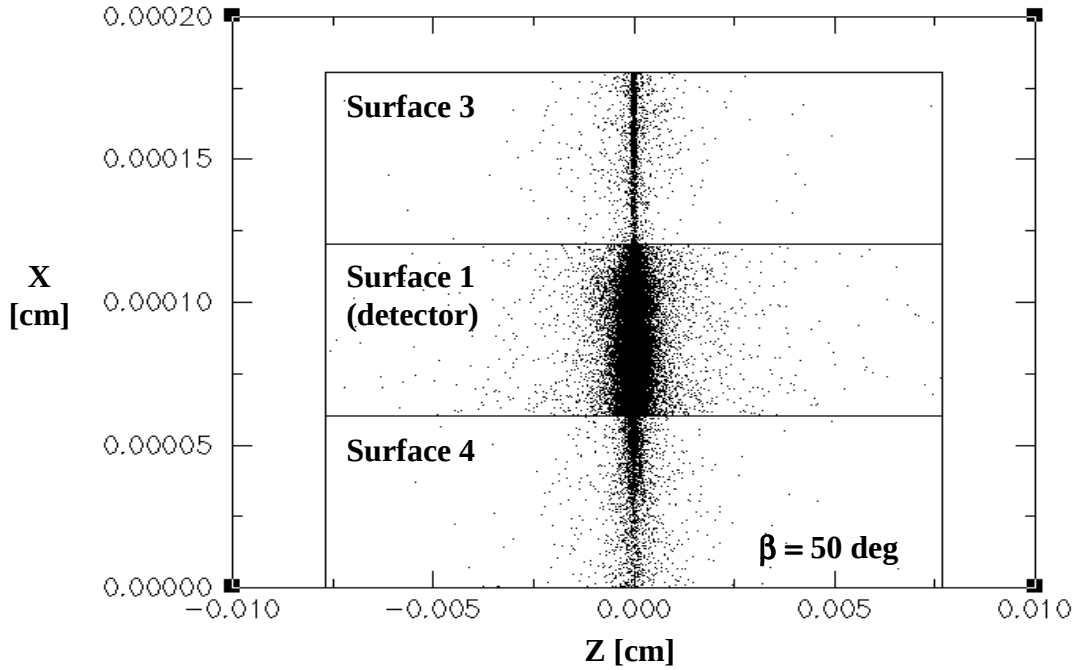

Figure 4.7 Scattergram of energy bundles absorbed by Surfaces 1,3, and 4 for a wedge angle of 50 deg (nominal values surface optical properties)

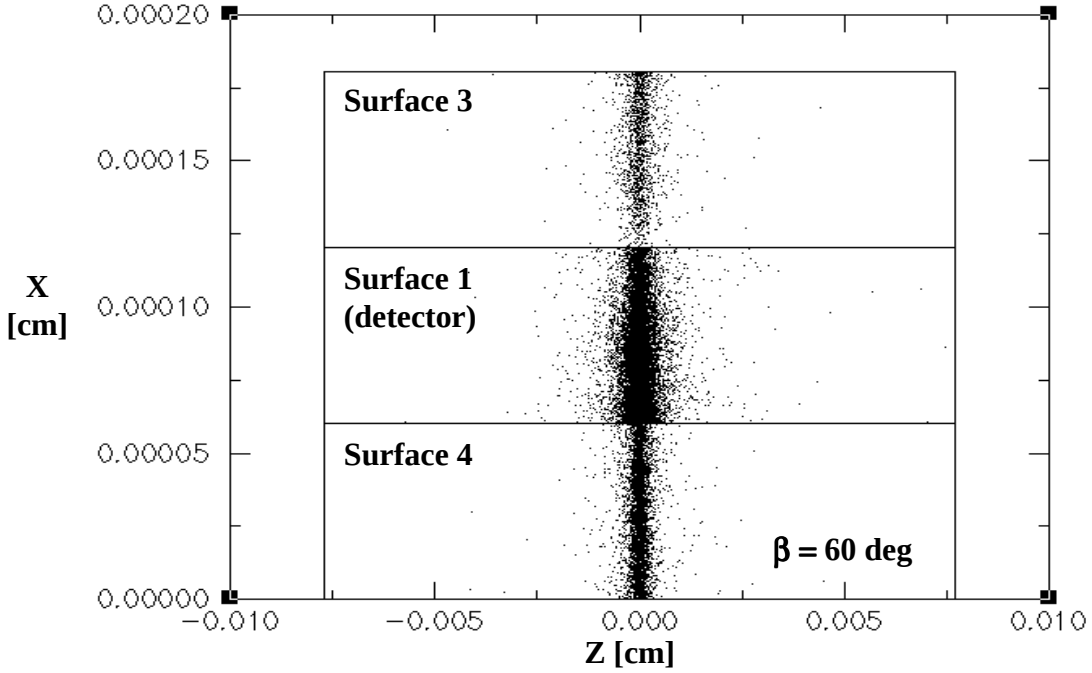

Figure 4.8 Scattergram of energy bundles absorbed in Surfaces 1, 3, and 4 for a wedge Angle of 60 deg (nominal values surface optical properties)

4.2.2 Taper Effect

In order to analyze and understand the taper effect, the program was modified to discard the energy bundles absorbed by the two central pixels (128 and 129) upon initial incidence; in other words, the energy bundles counted in this case are the energy bundles absorbed by the detector after at least one reflection occurs. Also, the detector was artificially divided into six horizontal (x-direction as defined in Figure 4.3) bands. In Figures 4.9 through 4.13 bar graphs show the number of energy bundles absorbed by each horizontal band in the detector. The number one (1) on the horizontal axis refers to the band on the bottom of the detector and number six (6) to the band at the top of the detector. The number printed at the top of each bar refers to the number of energy bundles absorbed in the band.

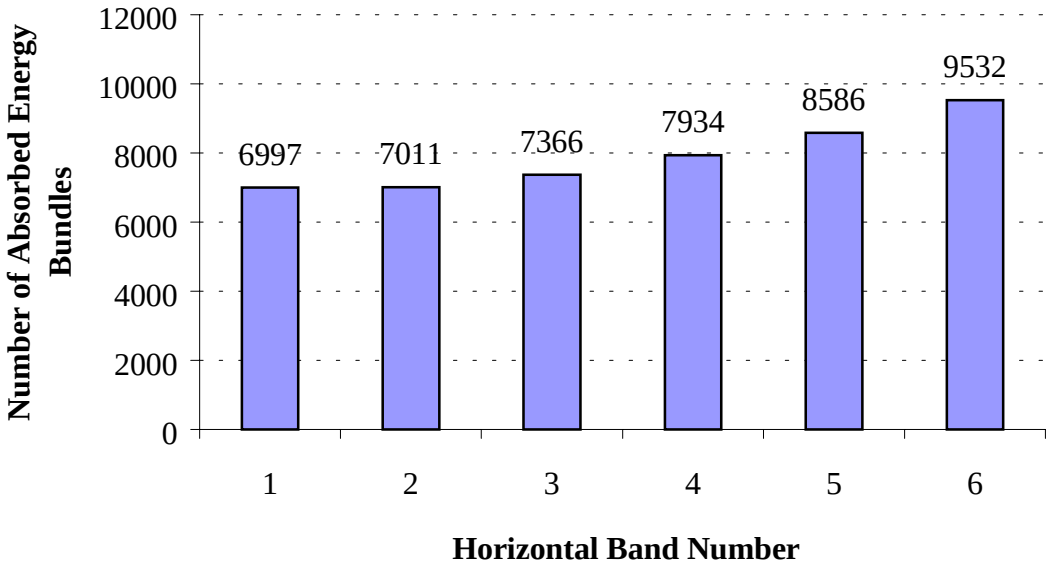

Figure 4.9 Illustration of the taper effect. Distribution of absorbed energy bundles by horizontal bands in the detector for a wedge angle of 30 deg (nominal values surface optical properties)

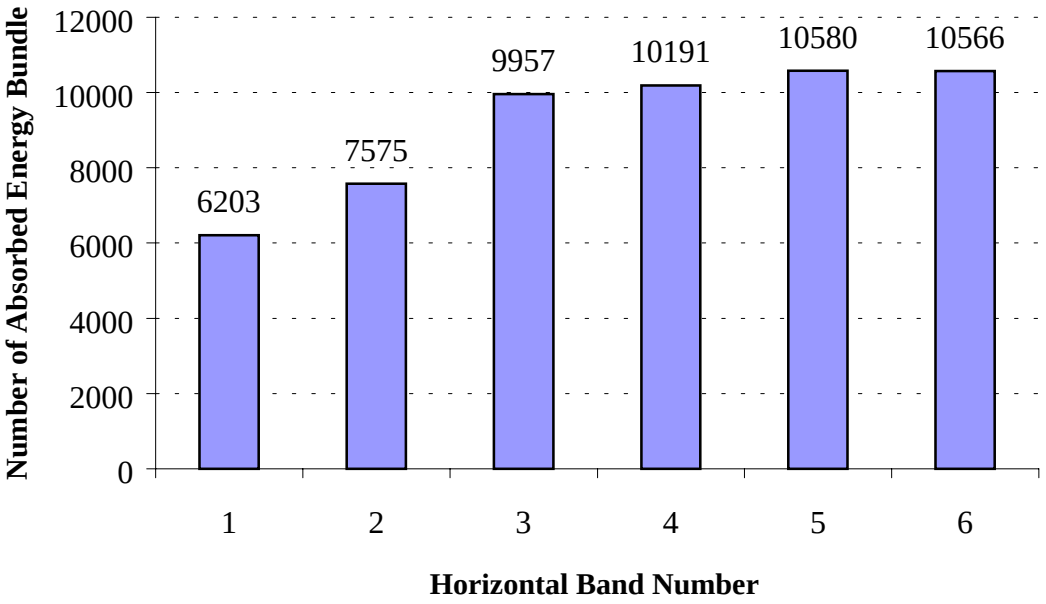

Figure 4.10 Illustration of the taper effect. Distribution of absorbed energy bundles by horizontal bands in the detector for a wedge angle of 40 deg (nominal values surface optical properties).

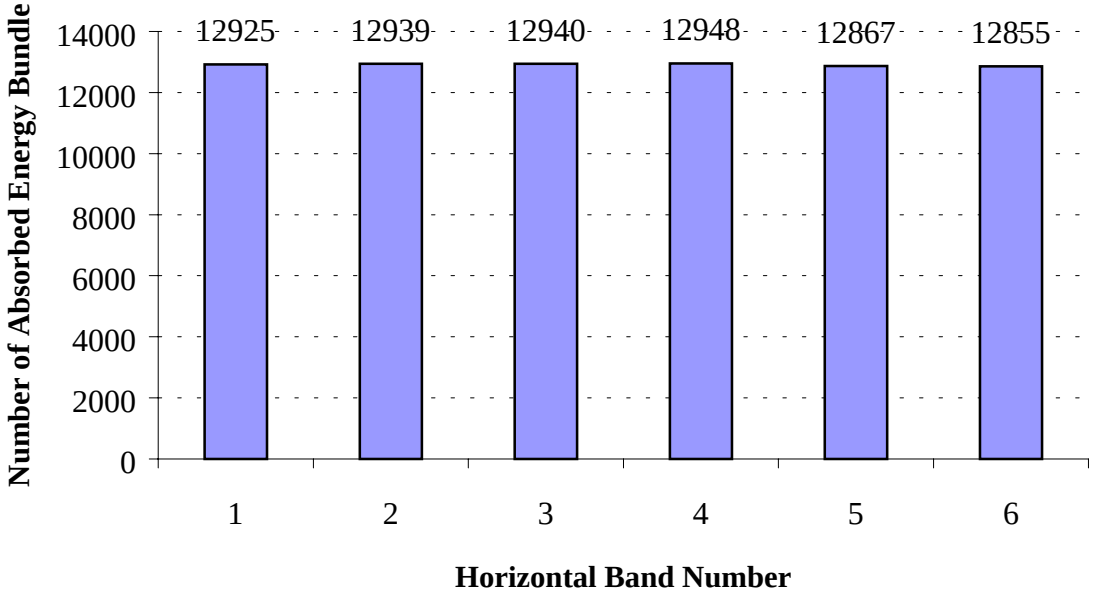

Figure 4.11 Illustration of the taper effect. Distribution of absorbed energy bundles by horizontal bands in the detector for a wedge angle of 45 deg (nominal values surface optical properties)

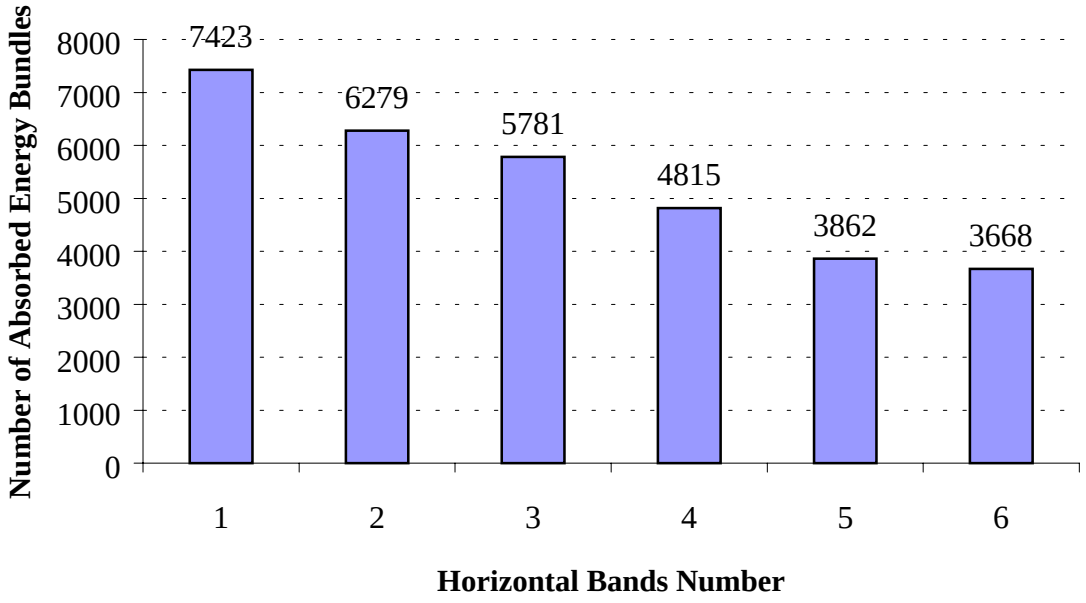

Figure 4.12 Illustration of the taper effect. Distribution of absorbed energy bundles by horizontal bands in the detector for a wedge angle of 50 deg (nominal values surface optical properties)

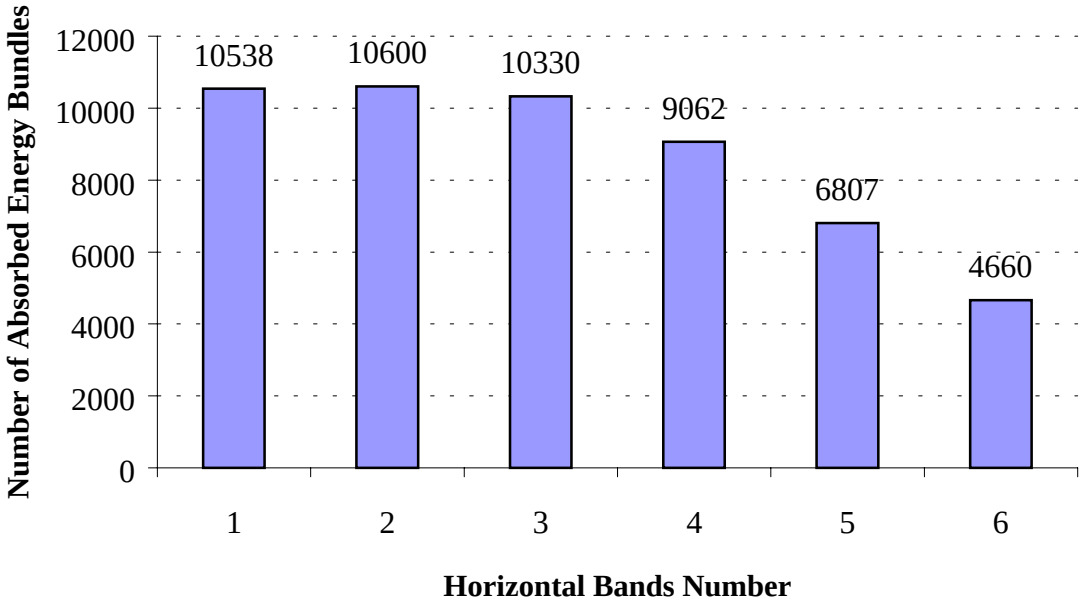

Figure 4.13 Illustration of the taper effect. Distribution of absorbed energy bundles by horizontal bands in the detector for a wedge angle of 60 deg (nominal values surface optical properties)

The bar graphs clearly show the change in the distribution of the absorbed energy bundles across the horizontal bands. For those angles tested below 45 deg, shown in Figures 4.9 and 4.10, a variation of the distribution of absorbed energy bundles across the horizontal bands is observed in which more energy bundles are absorbed at the bottom than at the top. In the case of β = 45 deg, Figure 4.11, uniformity over the horizontal divisions is presented. Also note that the number of absorbed energy bundles at this angle is higher than at all the other angles. For angles above 45 deg, shown in Figures 4.12 and 4.13, the distribution presents a decrease from the bottom to the top of the detector. It is clear from this part of the study that the maximum responsivity and the most efficient use of the linear-array detector surface area is achieved for a cavity wedge angle of 45 deg.

4.2.3 Distribution of Energy Bundles Absorbed by the Pixels

It is of interest to study the distribution of the energy bundles absorbed in each pixel along the entire detector. An analysis of the number of energy bundles absorbed in each of the 256 pixels of the detector is presented next. The program was modified to count the number of energy bundles absorbed after one or more reflections occur for different values of the wedge angle β. As before, only the two pixels in the middle of the detector are illuminated by direct radiation.

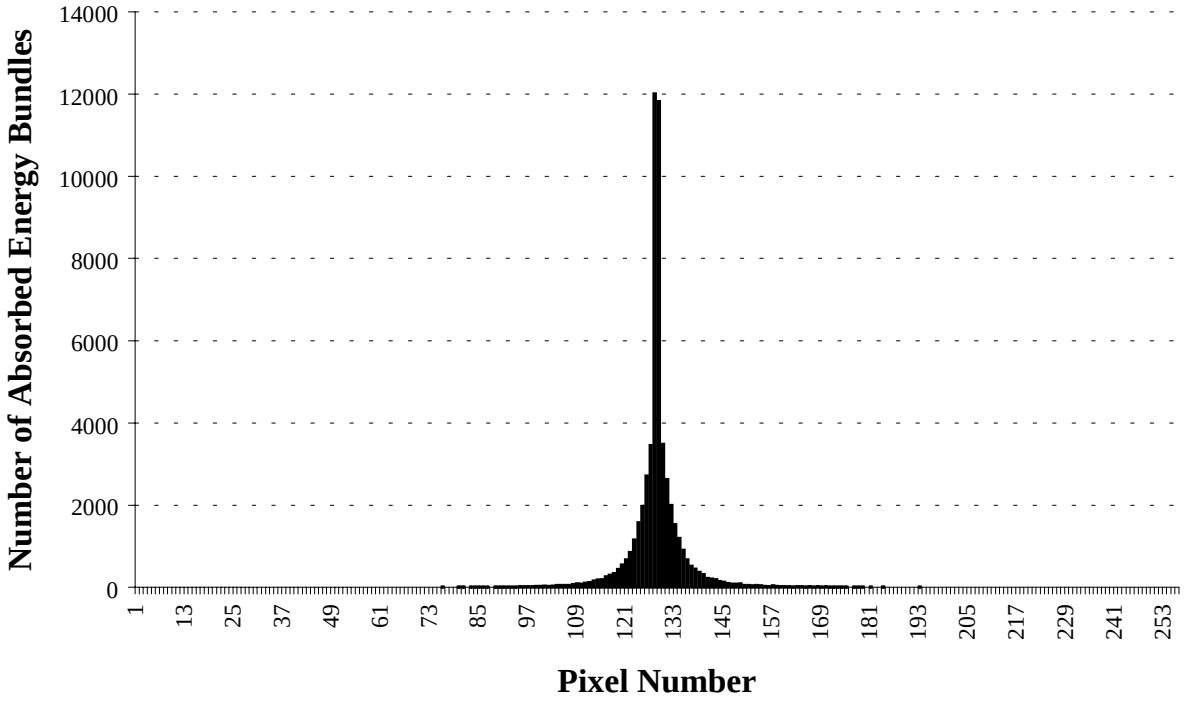

Figure 4.14 Number of energy bundles absorbed in each pixel for β = 30 deg (nominal values surface optical properties).

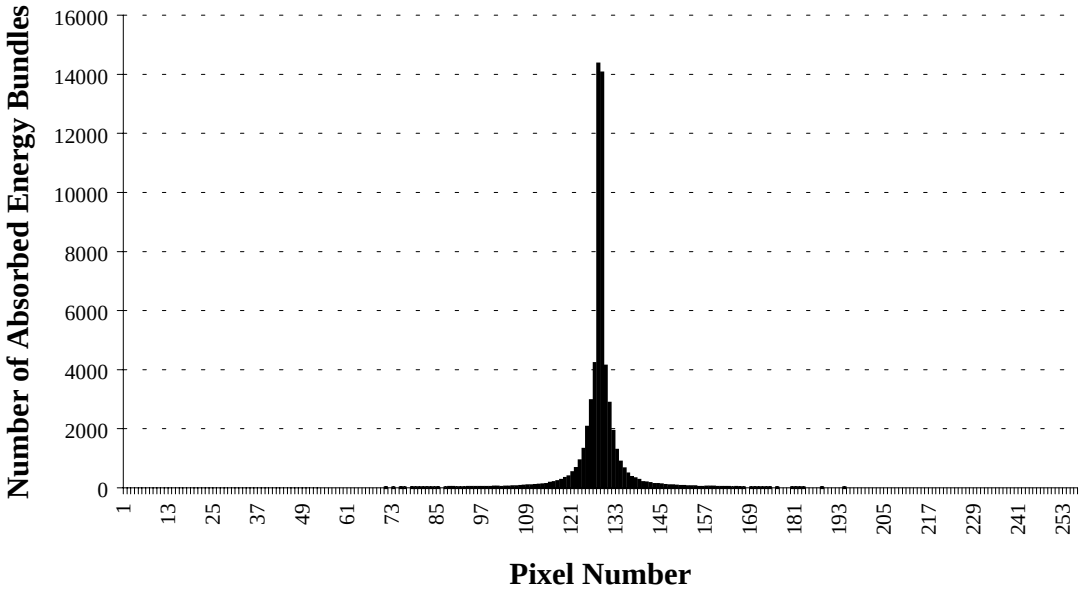

Figure 4.15 Number of energy bundles absorbed in each pixel for β = 40 deg (nominal values surface optical properties).

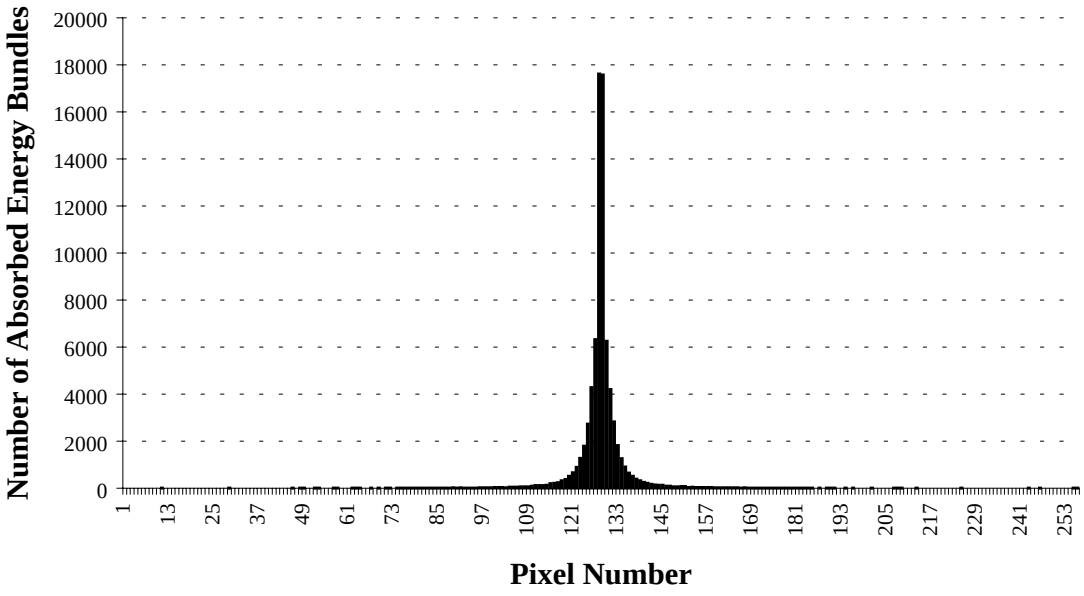

Figure 4.16 Number of energy bundles absorbed in each pixel for β = 45 deg (nominal values surface optical properties)

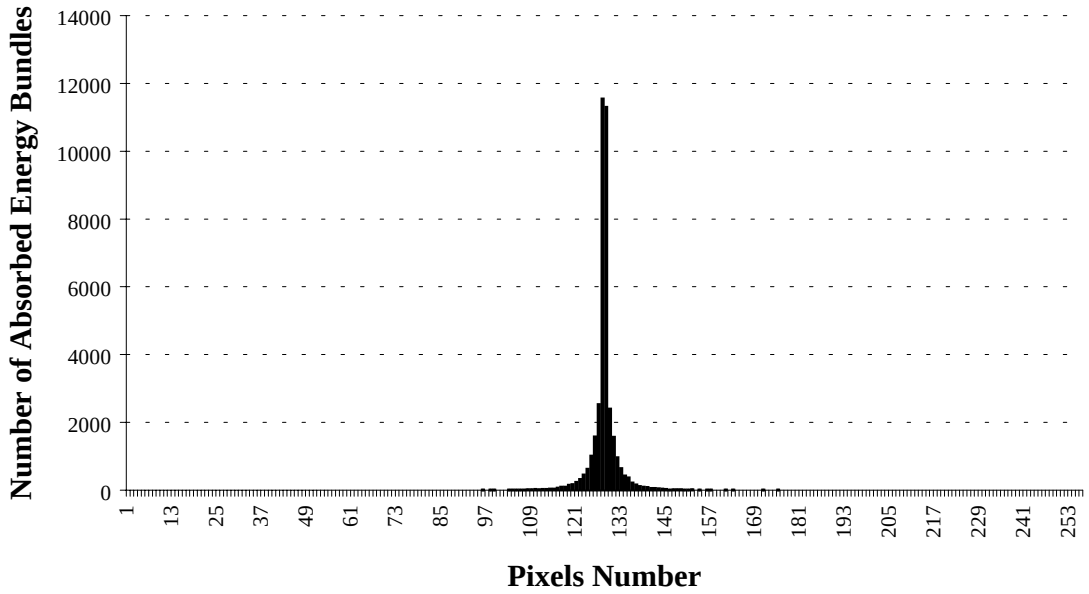

Figure 4.17 Number of energy bundles absorbed in each pixel for β = 50 deg (nominal values surface optical properties).

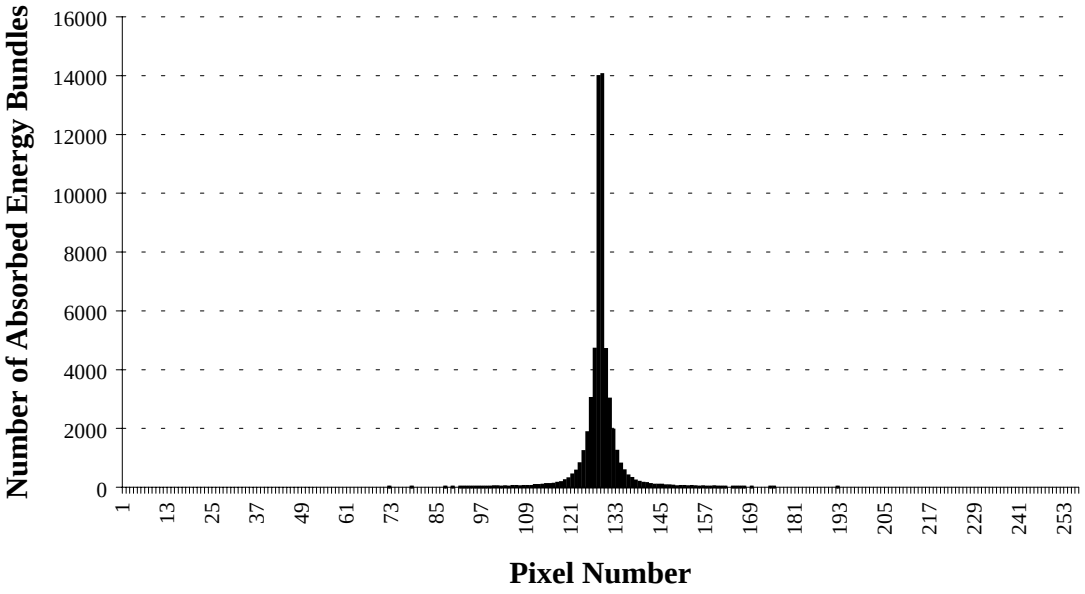

Figure 4.18 Number of energy bundles absorbed in each pixel for β = 60 deg (nominal values surface optical properties).

From Figures 4.14 through 4.18, it is possible to see the same tendency that was observed before on the vertical distribution of the energy bundles absorbed by the detector. When β = 45 deg (Figure 4.16), the number of energy bundles absorbed is higher than for the other angles. Also, at this angle the data are more widely distribuited over the detector and more symmetric around the two central pixels, thus confirming the uniformity established in the previous section. It is significant to note that when β = 60 deg the number of energy bundles absorbed is noticeably smaller than at other values of wedge angle.

4.2.4 Optical Cross-Talk

Figures 4.14 through 4.18 suggest a potentially very important application of the optical cross-talk results. Consider a beam of power h_i incident to a pixel i. Then the ultimate distribution of the radiation initially incident to this pixel absorbed on the pixels of the linear array is given by a discrete Green's function g'_{ij} defined such that

$$\sum_{i=1}^{n} h_i g'_{ij} = r_j, \qquad 1 \le j \le n \tag{4.6}$$

where r_j is the response of pixel j. Then if g'_{ij} is known the distribution of incident radiation can be recovered using

or
$$h_i = \left[g'_{ij}\right]^{-1} r_j, \qquad 1 \le i \le n \tag{4.7}$$

In other words we can use the discrete Green's function to deconvolve the data to recover the actual spatial distribution of radiation entering the slit of the detector. Figure 4.7 illustrates this concept schematically.

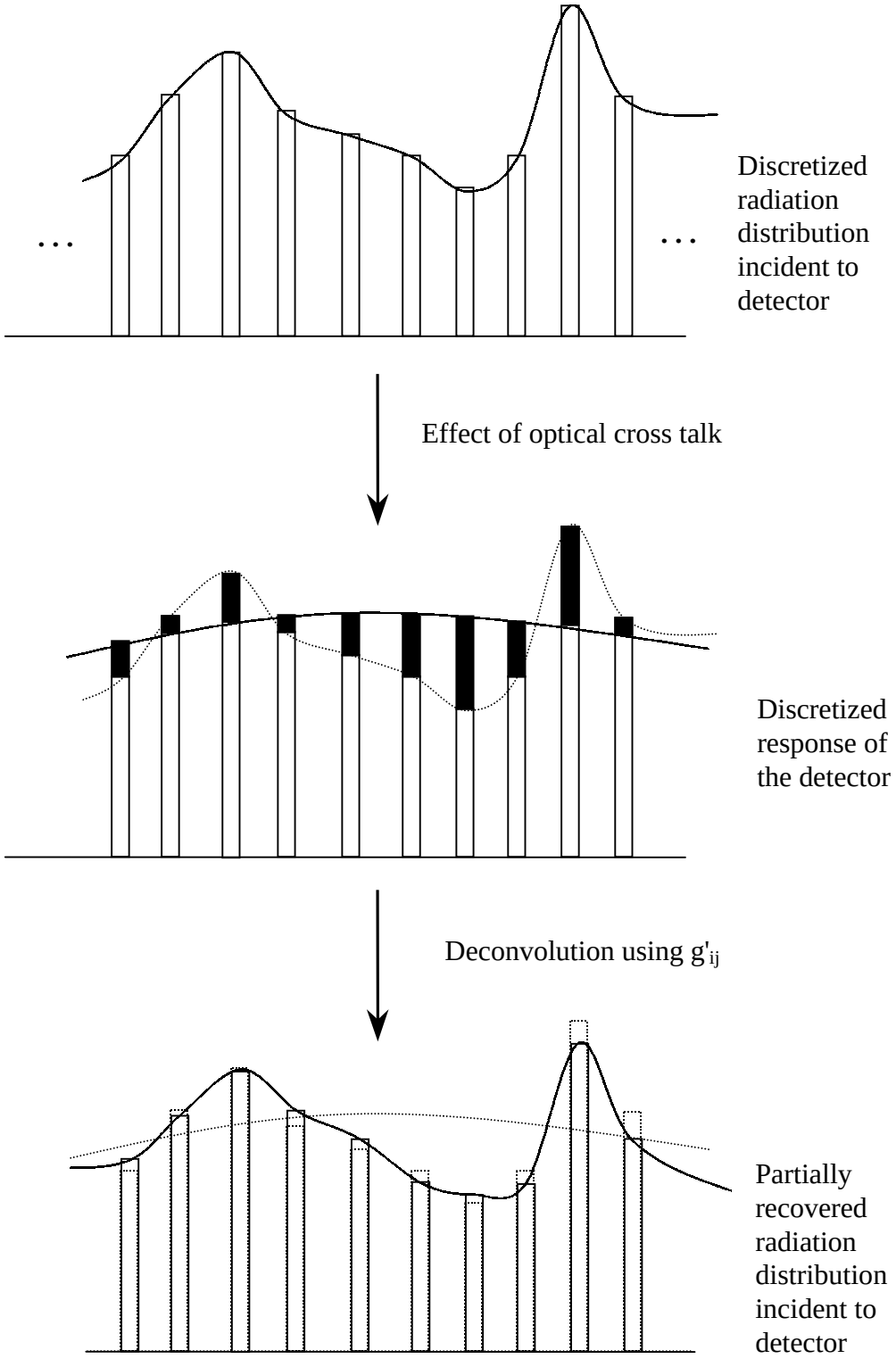

Figure 4.19 Schematic representation of use of the discrete Green's function g'_{ij} for deconvolution

4.2.5 Taper Effect on the Pixels

After studying the vertical taper effect over the detector (Sections 4.2.1 and 4.2.2), it is of interest to analyze the change in the distribution of the energy bundles absorbed by each pixel along the horizontal (z-direction) divisions of the detector with the change of the wedge angle. Because the bar graphs shown in Figures 4.14 through 4.18 are very similar for every horizontal band and do not offer a good discrimination of the results, Table 4.2, showing some basic statistics of the data, is provided. For this case, the pixels number are shifted so that zero is at the center of the detector. Figure 4.20 shows a schematic representation of these statistical calculations. The values of the mean and standard deviation in Table 4.2 are calculated using

$$\langle i \rangle = \sum_{i=-128}^{128} i\, n_i \tag{4.8}$$

and

$$s = \sqrt{\sum_{i=-128}^{128} (i - \langle i \rangle)^2\, n_i}\ , \tag{4.9}$$

where

$$n_i \equiv \frac{N_i}{\sum_{i=-128}^{128} N_i}. \tag{4.10}$$

In Equation 4.10 N_i is the number of energy bundles absorbed by the i^{th} pixel.

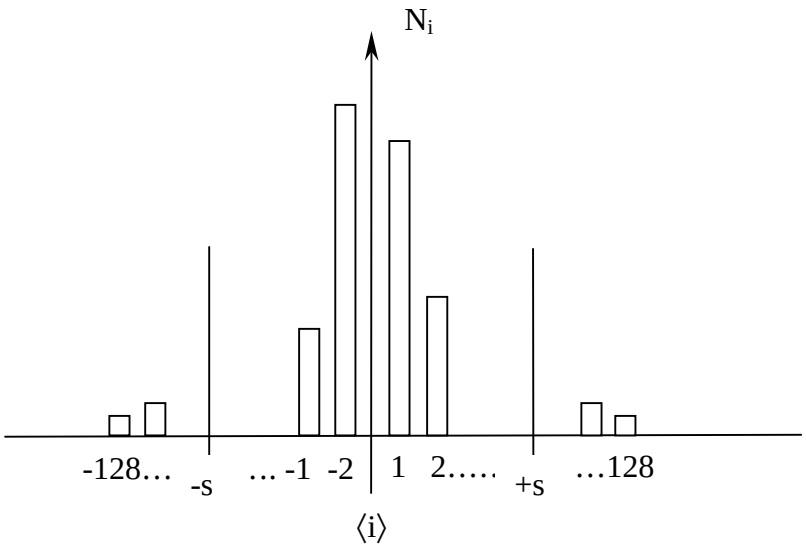

Figure 4.20 Schematic representation of the statistics calculations whose results are given in Table 4.2 (nominal values surface optical properties)

Note that all the values for the mean in Table 4.2 are near zero, which is the hypothesis of Equation 4.6 in Section 4.1. The standard deviation is seen to vary from around 4 pixels to 11 pixels. The highest value for the standard deviation occurs when β = 45 deg, but this is also the angle for which the detector absorbs the most energy bundles.

The standard deviation in terms of pixel number is plotted in Figures 4.21 and 4.22. These graphs show the scattering of the absorbed energy bundles in the detector. In Figure 4.21 the standard deviation is plotted for each angle with respect to the number of the horizontal band. It is clearly seen that the values for β = 45 deg are higher and again, more uniform, than for the other angles. In Figure 4.22 the standard deviation is shown as function of the angle for each vertical band.

Table 4.2 Basic statistics of taper effect in each pixel

β	Number. Horizontal Band	Mean [pixels]	Standard Deviation [pixels]	Number of. Absorbed Energy Bundles
30°	1	-0.10947	8.48543	6997
	2	0.10526	9.13287	7011
	3	0.12721	7.94944	7366
	4	-0.00819	7.81909	7934
	5	-0.00932	7.43951	8586
	6	0.11456	6.78702	9532
40°	1	0.28728	9.76718	6203
	2	-0.0697	8.79985	7575
	3	-0.09601	7.65876	9957
	4	0.02512	8.23137	10191
	5	-0.13913	7.9978	10580
	6	0.00965	7.99931	10566
45°	1	0.18548	10.92105	12923
	2	-0.04019	10.68722	12938
	3	-0.09893	10.92248	12939
	4	0.11091	10.34205	12947
	5	0.06553	11.03345	12865
	6	0.03469	10.4854	12855
50°	1	-0.02287	6.73911	10538
	2	0.01472	6.23834	10600
	3	0.00300	5.6975	10330
	4	0.09291	6.52772	9062
	5	-0.01322	6.52028	6807
	6	0.26588	7.13922	4660
60°	1	0.00983	4.88929	7423
	2	0.02676	4.15992	6279
	3	-0.00346	4.43504	5781
	4	0.05213	4.21569	4815
	5	0.00906	4.54971	3862
	6	0.12568	4.37828	3668

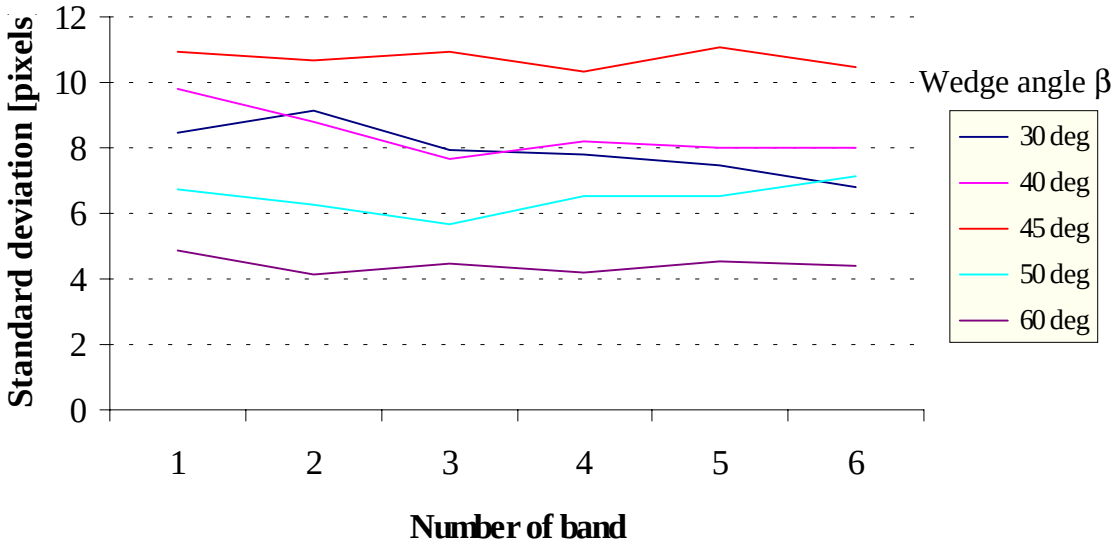

Figure 4.21 Standard deviation of the energy bundles absorbed by each pixel in every horizontal band for different values of wedge angle β (nominal values surface optical properties).

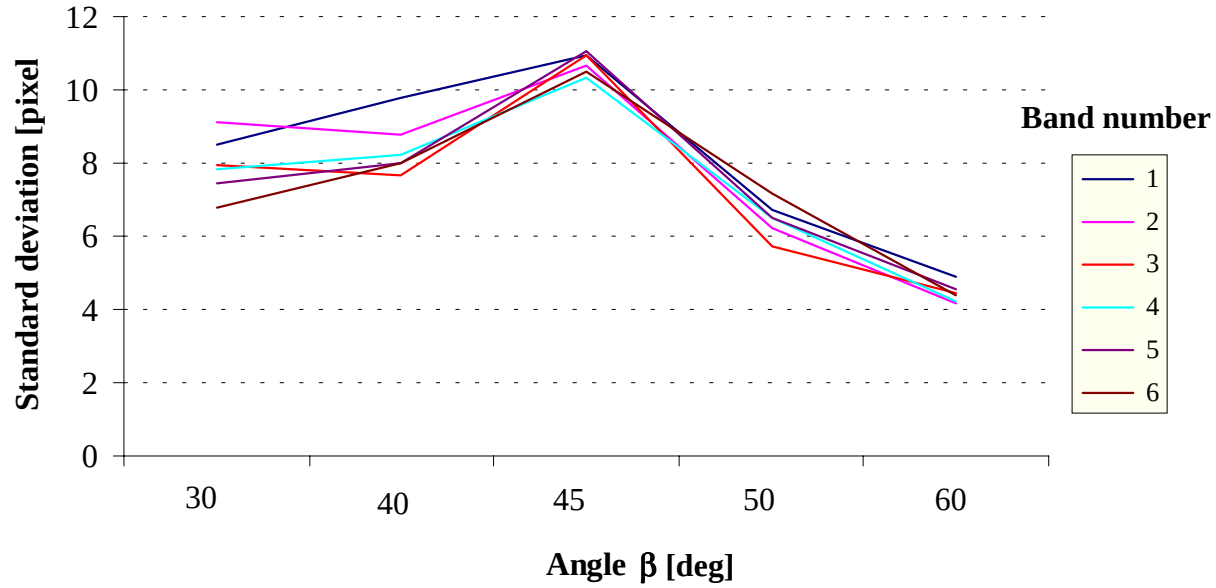

Figure 4.22 Standard deviation of the energy bundles absorbed by each pixel as a function of the wedge angle for every horizontal band (nominal values surface optical properties)

4.2.6 Effects of the Surfaces Properties

In order to optimize the design of the GERB thermal radiation detector concept, a study of the effect that the surface optical properties have on the instrument is necessary. Small modifications in the Subroutine PROPERTIES allow displaying the number of energy bundles absorbed inside the cavity as well as the position where they are absorbed. The following study was made using a value of 45 deg for the wedge angle β and illuminating only the two pixels in the center of the detector. The program counts only the energy bundles absorbed after one or more reflections occur.

Figures 4.23 (a), (b), and (c) show the effect on the distribution of absorbed energy bundles of changing the specularity ratio of the mirror-like walls. In other words, they show the effect of the trade-off between diffuse and mirror-like reflections. In these scattergrams the locations where the energy bundles are absorbed by Surfaces 1 (detector array), 3, and 4 are presented. It is emphasized that the overall reflectivity ($\rho^s + \rho^d$), and thus the absorptivity is held constant as the specularity ratio $\rho^s /(\rho^s + \rho^d)$ is varied

Note that as the specularity ratio increases (more mirror-like), the number of energy bundles absorbed by Surfaces 3 and 4 decreases. Because the specularity ratio is a measure of the probability that a surface reflects specularly, this means that when it increases the probability of diffuse reflections decreases and so less scattering to Surfaces 3 and 4 occurs.

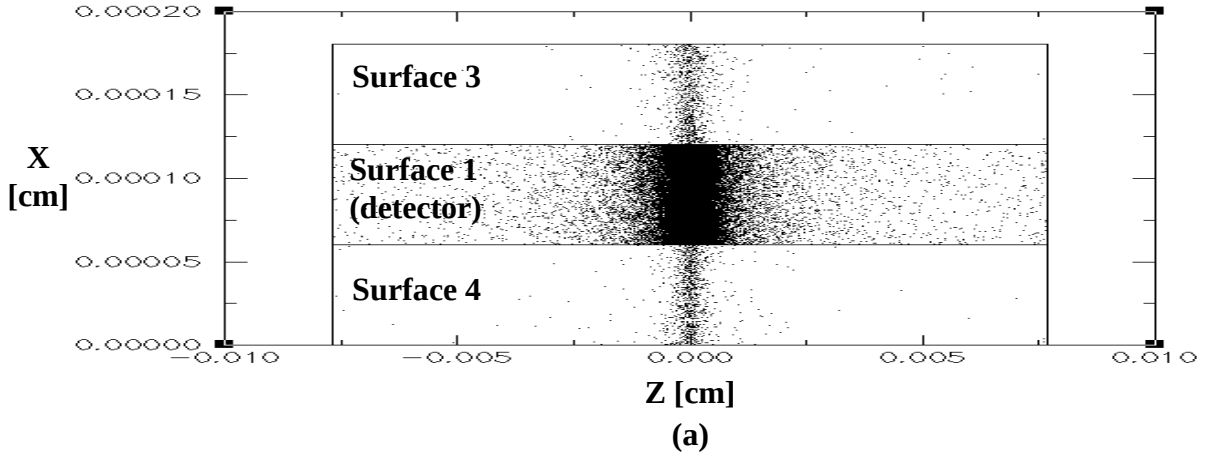

(a)

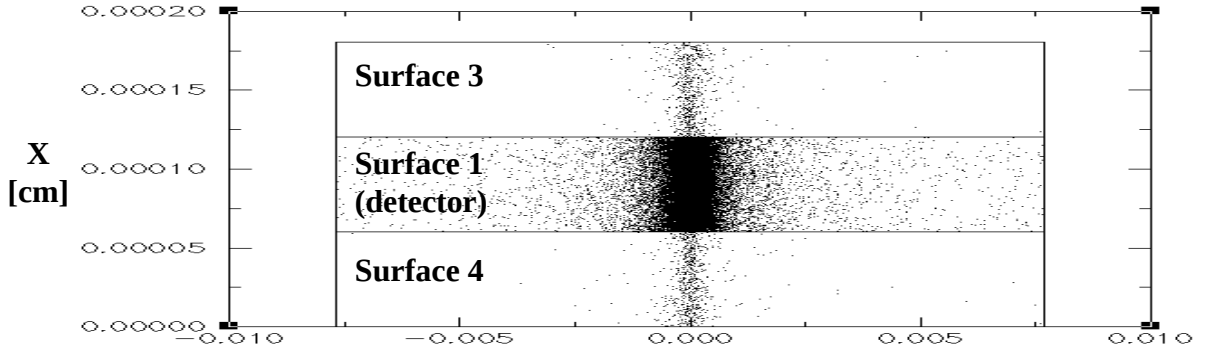

(b)

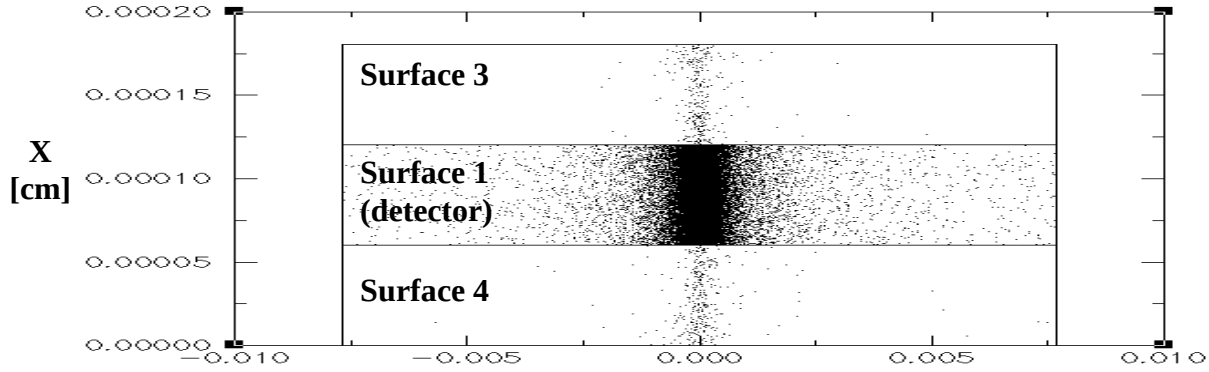

(c)

Figure 4.23 Energy bundles absorbed by Surfaces 1, 3, and 4 for mirror-like walls specularity ratio of (a) 0.85, (b) 0.90, and (c) 0.95 (nominal values surface optical properties)

In order to facilitate the analysis of the results in this section, a particular concept is introduce to measure the change in perfomance that occurs when the properties are changed. This concept, called the OCT_i coefficient for pixel i, is defined as

$$OCT_i = \frac{\text{Number of Energy Bundles Absorbed in Pixel i}}{\text{Mean number of the Energy Bundles Absorbed in the two central Pixels}}. \qquad (4.11)$$

Here OCT stands for "optical cross-talk". In general, a successful design will minimize optical cross-talk. If OCT_i decreases when the properties are changed, it means that the detector performance has improved. On the other hand, if OCT_i increases, the performance of the detector decreases.

In Table 4.3 values of the OCT_i are presented for several pixels near the center of the detector when the absorptivity ratio is changed.

Table 4.3 Values of OCT_i for different values of r_s in the mirror-like walls

Pixel Number	**r_s = 0.85**	**r_s = 0.90**	**r_s = 0.95**
124	0.10493	0.10376	0.10501
125	0.15348	0.15643	0.15796
126	0.23956	0.24393	0.24479
127	0.35168	0.35496	0.35797
128	1.00220	1.00023	1.00234
129	0.99785	0.99977	0.99766
130	0.35087	0.35411	0.35341
131	0.23846	0.23962	0.24173
132	0.16038	0.16109	0.16186
133	0.10423	0.10467	0.10262

In most of the cases OCT_i increases slightly when the specularity ratio increases. However, these changes are very small and in some cases there is no significant change in the detector performance. This means that optical cross-talk is fairly insensitive to specularity ratio of the mirrored walls for higher values of r_s. This is a mildly surprising and somewhat favorable result because the specularity ratio may prove to be difficult to measure accurately in a practical instrument. Also, the value may degrade slightly during prolonged exposure to the space environment.

Figures 4.24 show the location where the energy bundles are absorbed by Surfaces 1, 3, and 4 when the value of the absorptivity of the mirror-like walls is changed. Since the absorptivity in the detector array itself is maintained constant, the interest of this analysis is directed to the walls of the cavity. Looking carefully it is possible to see the small changes in absorption by Surfaces 3 and 4. More energy bundles are absorbed in those surfaces as the absorptivity increases, especially on the line of the center of the detector.

Table 4.4 presents the values of OCT_i for the ten central pixels for three different values of the absorptivity in the mirror-like walls. In this case OCT_i decreases when the absorptivity in the walls increases, as expected. Note that the changes in this table are more significant than in the previous table. This time OCT_i changes by about seven percent when the absorptivity doubles from 0.05 to 0.10 (see for example pixel number 125)

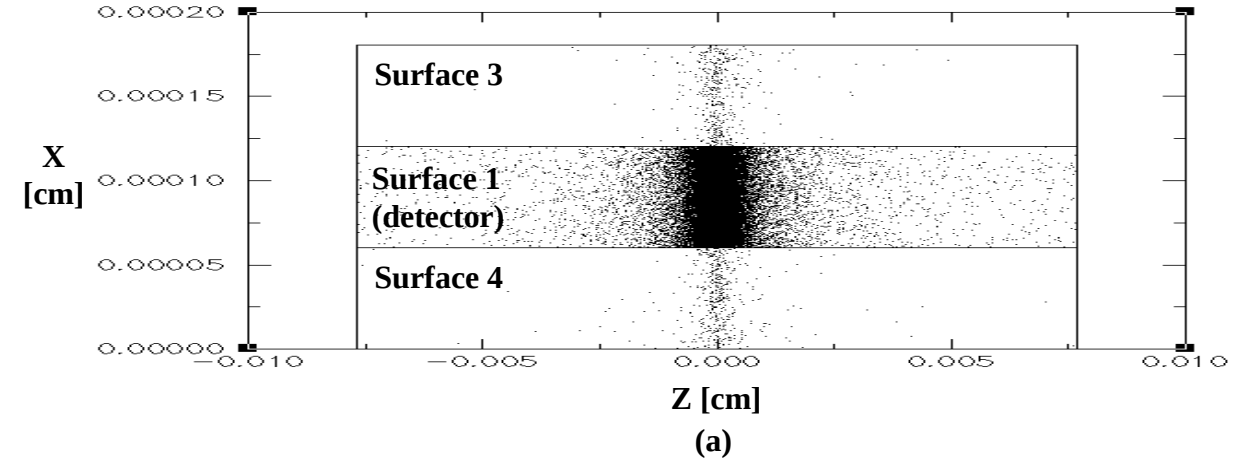

(a)

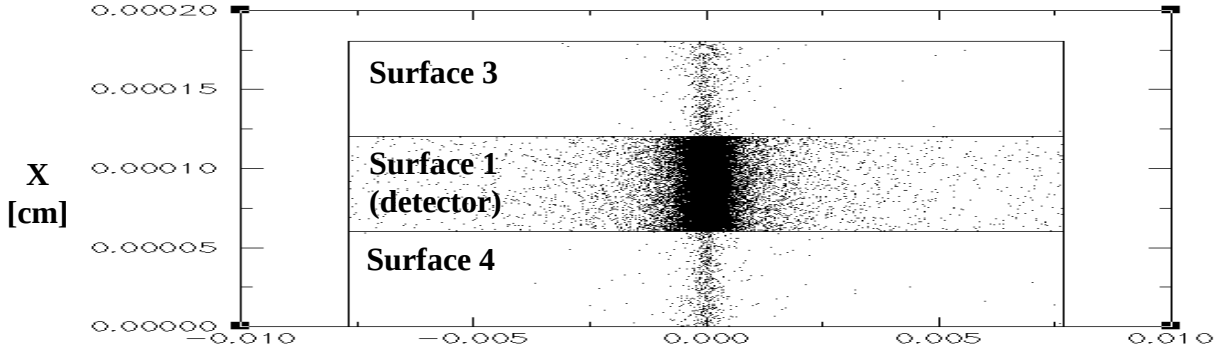

(b)

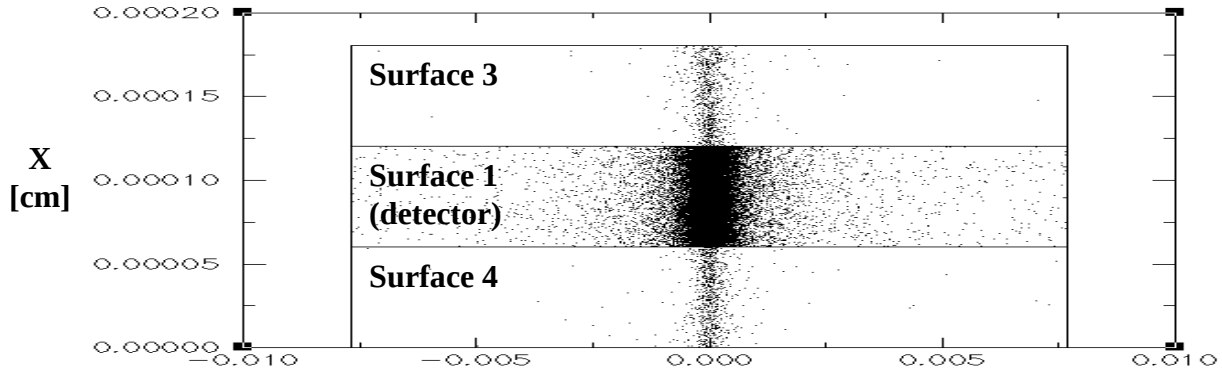

(c)

Figure 4.24 Energy bundles absorbed by Surfaces 1,3, and 4 for absorptivity in the mirror-like walls of (a) 0.05, (b) 0.10, and (c) 0.15 (nominal values surface optical properties)

Table 4.4 Values of OCT_i for different values of absorptivity α_w in the mirror-like walls

Pixel Number	**α_w = 0.05**	**α_w = 0.10**	**α_w = 0.15**
124	0.111976	0.103756	0.0957
125	0.167244	0.156429	0.146703
126	0.260779	0.243934	0.227465
127	0.376752	0.354963	0.332668
128	0.999201	1.000227	1.000968
129	1.000799	0.999773	0.999093
130	0.375793	0.354111	0.329462
131	0.257315	0.239616	0.225106
132	0.172041	0.161089	0.147247
133	0.113841	0.104665	0.09560

Following are the results of a study made in which the absorptivity of the thermal radiation detector was varied. First, Figure 4.25 shows the location where the energy bundles are absorbed by Surfaces 1, 3, and 4 for three values of absorptivity of the linear-array detector. In these scattergrams it is possible to see clearly the effect that the increment in the absorptivity of the detector has on the distribution of the absorbed energy bundles. When the absorptivity is lower, the data tend to spread out over the detector. Also, the number of energy bundles absorbed along the central vertical axis of the plane is greater than when the absorptivity is higher.

Table 4.5 shows that except for the two central pixels in the middle (pixels number 128 and 129) the value of OCT_i decreases when the absorptivity increases. This means that an effective means of minimizing the optical cross-talk is to maximize the absorptivity of the linear-array detector.

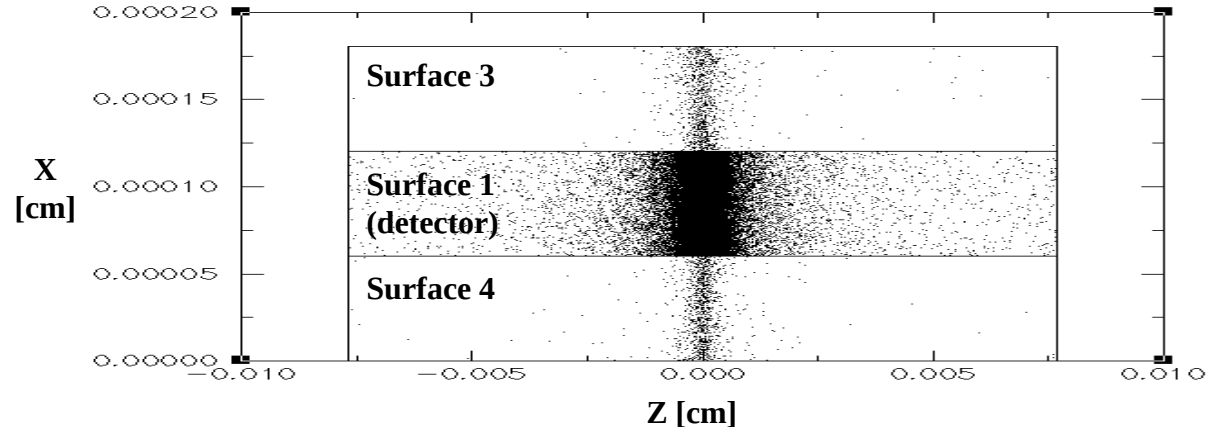

(a)

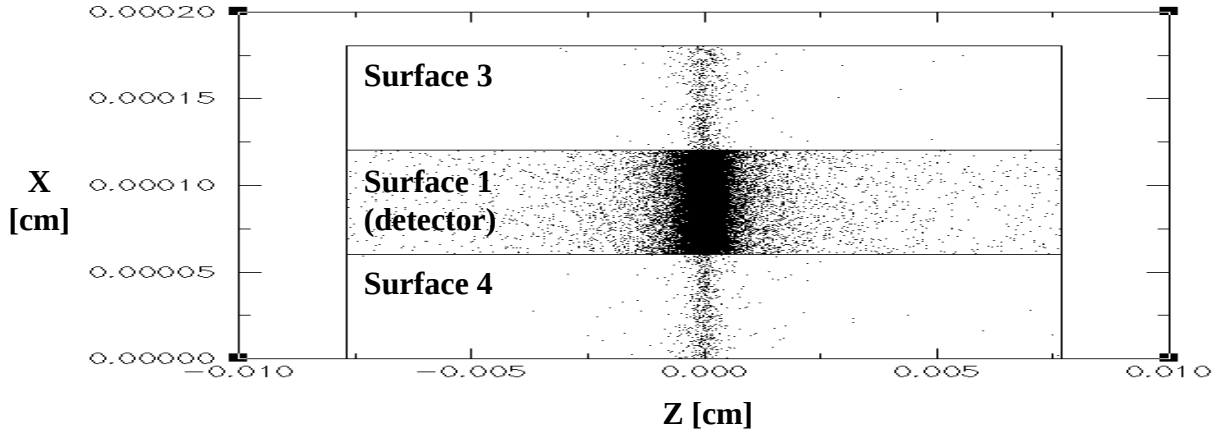

(b)

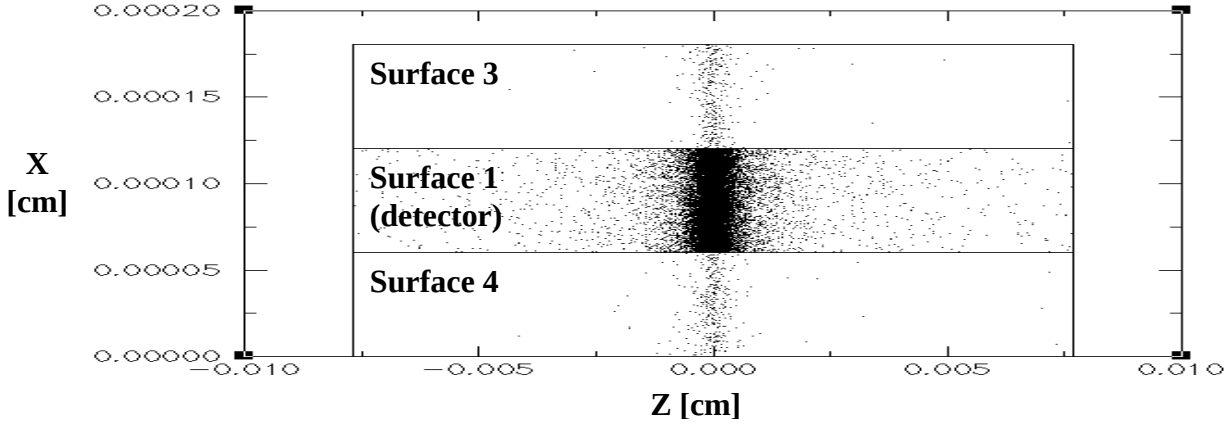

(c)

Figure 4.25 Energy bundles absorbed by surfaces 1, 3, and 4 for linear-array surface absorptivity of (a) 0.85, (b) 0.90, and (c) 0.95 (nominal values surface optical properties)

Table 4.5 Values of OCT_i for different values of absorptivity α_d of the detector

Pixel Number	**α_d= 0.85**	**α_d= 0.90**	**α_d= 0.95**
124	0.112579	0.103756	0.100895
125	0.168513	0.156429	0.150251
126	0.245926	0.243934	0.233675
127	0.363608	0.354963	0.340358
128	1.003916	1.000227	1.004477
129	0.996123	0.999773	0.995632
130	0.356606	0.354111	0.341123
131	0.2536	0.239616	0.233785
132	0.165665	0.161089	0.154182
133	0.108149	0.104665	0.100022

Chapter 5. Conclusions and Recommendations

5.1 Conclusions

From the results obtained in this thesis it may be concluded that:

1. The numerical model developed in this thesis is a valuable tool for the optimization of the design of linear-array thermal radiation detectors of the type proposed for GERB.
2. The results from the study of the influence of the wedge angle β show that at 45 deg the vertical uniformity of the distribution of absorbed energy bundles over the detector is highest. At the same angle, the greatest number of energy bundles is absorbed. Unfortunately, 45 deg is also the angle that produces the greatest horizontal scatter (cross-talk) of the data.
3. Changes in the surface optical properties produce principally changes in the horizontal distribution of the absorbed energy bundles.
4. When the specularity ratio in the mirror–like surfaces is increased, the horizontal scatter in Surfaces 3 and 4 decreases. If the absorptivity in the same surfaces is increased, the optical cross-talk on these surfaces and on the detector itself also increases.
5. Increases in the absorptivity of the detector result in a decrease of the horizontal scatter over the detector as well as in the horizontal scatter on the adjacent surfaces (Surfaces 3 and 4).
6. Using the model it is possible to estimate the discrete Green's function which may be used to recover the incident spatial distribution of radiation entering the cavity.

5.2 Recommendations

1. It is recommended that a value for the wedge angle β of 45 deg be used in future designs.
2. A combination of high specularity ratio and small absorption on the mirror-like surfaces, and high absorptivity on the detector is recommended to minimize optical cross-talk
3. Incorporation of a complete analysis of the diffraction phenomenon in the cavity would improve the credibility of the optical model.
4. The optical analysis presented in this thesis should be combined with the dynamic electrothermal model of the thermopile detector presented by Weckmann [1997] in her master's thesis.
5. The discrete Green's functions g'_{ij} should be estimated and a study undertaken to determine the ability to recover the spatial distribution of radiation incident to the slit.
6. The model should be expanded to include the ability of performing a thermal self-contamination study.

REFERENCES

1. Anon., 1996. http://www.noaa.gov/public-affairs/pr96/jan96/satgoesback.html

2. Anon., 1997 *a*. http://daac.gsfc.nasa.gov/PLATFORM_DOCS/UARS_platform.html

3. Anon., 1997 *b*. http://stud2.tuwien.ac.at/~e9527412

4. Anon., 1997 *c*. http://www.sp.ph.ic.ac.uk/~johannes/GERB.html

5. Clouds and the Earth's Radiant Energy (CERES) Preliminary Design Review, June 25, 1992. TRW Space & Technology Group. Applied Technology Division. Document No. 55067.100.018, DRL 47, pp PJ23

6. Bongiovi, Robert P. II, **A Parametric Study of the Radiative and Optical Characteristics of a Scanning Radiometer for Earth Radiation Budget Applications Using the Monte-Carlo Method.** Master of Science Thesis, Mechanical Engineering Department, Virginia Polytechnic Institute and State University, Blacksburg, VA 1993

7. Barkstrom, B.R., *Earth Radiation Budget Measurements: pre-ERBE, ERBE and CERES,* **Proceeding of SPIE-The International Society for Optical Engineering,** Vol. 1299, 1990, pp 52-60.

8. Hogg, Robert V. and Johannes Ledolter, **Applied Statistics for Engineers and Physical Scientists,** Macmillan Publishing Company, 1987

9. House, F.B., A. Gruber, G.E. Hunt, and A.T. Mecherikunnel, *History of Satellite Missions and Measurements of the Earth Radiation Budget (1957-1984),* **Reviews of Geophysics,** Vol. 24, No. 2, May 1986, pp 357-377.

10. Hunt, G.E., R. Kandel, and A.T. Mecherikunnel, *A History of Presatellite Investigations of the Earth's Radiation Budget.* **Reviews of Geophysics,** Vol. 24, No. 2, May 1986, pp 351-356.

11. Koopmans, Lambert H, **Introduction to Contemporary Statistical Method**. Prendall Weber & Schmidt Publisher. Duxbury. Second edition. 1987

12. Kopia, L.P., *Earth Radiation Budget Experiment Scanner Instrument,* **Reviews of Geophysics,** Vol. 24, No.2, May 1986, pp 400-406.

13. Mahan, J.R., and L.D. Eskin, *The Radiation Distribution Factor - Its Calculation Using Monte Carlo and Example of its Aplication,* **First UK National Heat Transfer Conference,** July 4-6, 1984, Leeds, Yorkshire, England, pp 1001-1012.

14. Mahan, J.R., and L.W. Langley, **The Geo-Synchronous Earth Radiation Budget Instrument: A Thermopile Linear-Array Thermal Radiation Detector,** Proposal submitted to NASA, Hampton, VA, 1996.

15. Mahan, J. R., and L.W. Langley, **Technology Development of a Sputtered Thermopile Thermal Radiation Detector for Earth Radiation Budget Applications,** Proposal submitted to NASA, Hampton, VA, 1997.

16. Mahan, J. R., **Radiation Heat Transfer A Modern Approach,** Spring 1998, [Manuscript].

17. Meekins, Jeffrey L., **Optical Analysis of the ERBE Scanning Thermistor Bolometer Radiometer Using the Monte Carlo Method,** Master of Science Thesis, Mechanical Engineering Department, Virginia Polytechnic Institute and State University, Blacksburg, VA,1996

18. Nguyen, Tai K., **Optimization of Radiometric Channel Solar Calibration for the Clouds and the Earth's Radiant Energy System (CERES) Using the Monte-Carlo Method,** Master of Science thesis, Mechanical Engineering Department, Virginia Polytechnic Institute and State University, Blacksburg, VA,1996

19. Nyhoff, Larry, Sanford Leestma, **FORTRAN 77 for Engineering and Scientists,** Third Edition, Macmillan Publishing Company, 1992.

20. Sparrow, E.M., E.R.G. Eckert, and V.K. Jonsson, *An Enclosure Theory for Radiative Exchange Between Specularly and Diffusely Reflecting Surfaces,* **Journal of Heat Transfer,** Vol. 84, No. 11, November 1962, pp 294-300

21. Sparrow, E.M., and R.D. Cess, **Radiation Heat Transfer,** Wadsorth Publishing Company, Inc., 1966

22. Turk, Jeffrey A., **Acceleration Techniques for the Radiative Analysis of General Computational Fluids Dynamics Solutions Using Reverse Monte-Carlo Ray Tracing.** Ph.D. Dissertation, Mechanical Engineering Department, Virginia Polytechnic Institute and State University, Blacksburg, VA,1994

23. Walkup, Michael D., **A Monte-Carlo Optical Workbench for Radiometric Imaging System Design,** Master of Science Thesis, Mechanical Engineering

Department, Virginia Polytechnic Institute and State University, Blacksburg, VA,1996

24. Walpole, Ronald E., and Raymond H. Myers, **Probability and Statistics for Engineers and Scientists,** Macmillan Publishing Company. Fifth edition, 1993

25. Weckmann, Stephanie, **Dynamic Electrothermal Model of a Sputtered Thermopile Thermal Radiation Detector for Earth Radiation Budget Applications,** Master of Science Thesis, Mechanical Engineering Department, Virginia Polytechnic Institute and State University, Blacksburg, VA, 1997

26. Wielicki, B.A., R.D. Cess, M.D. King, and E.F. Harrison, *Mission to Planet Earth: Role of Clouds and Radiation in Climate*, **Bulletin of American Meteorological Society.** Vol. 76, No. 11, November 1995, pp 2125-2153.

27. Wielicki, B.A., Bruce R. Barkstrom, Edwin F. Harrison, Robert B. Lee III, G. Louis Smith, and John E. Cooper, *Clouds and the Earth's Radiant Energy System (CERES): An Earth Observing System Experiment*, **Bulletin of the American Meteorological Society.** Vol. 77, No. 5, May 1996, pp 853-868

Vita

María Cristina Sánchez was born on the 4th day of February, 1972, in Santa Fé de Bogotá, Colombia. She moved to Neiva (Huila) where she spent her formative years. She graduated from *Colegio Cooperativo Campestre* high school in 1988 and was accepted to *La Universidad de los Andes* in Santa Fé de Bogotá where she received her bachelor's degree in Mechanical Engineering in 1996. She then moved to the United States to enroll in the master's program at Virginia Polytechnic Institute and State University, where she works as a research assistant in the Thermal Radiation Group. After finishing her Masters, she will take part in a doctoral exchange program with the Universidad Politécnica de Puerto Rico.

María Cristina Sánchez C.